



Delft University of Technology

Large-eddy simulation of dual-fuel spray ignition at varying levels of methane diluted ambient oxidizer using FGM

Bao, Hesheng; Han, Jinlin; Zhang, Yan; Di Matteo, Andrea; Roekaerts, Dirk; Van Oijen, Jeroen; Somers, Bart

DOI

[10.1016/j.fuel.2023.128901](https://doi.org/10.1016/j.fuel.2023.128901)

Publication date

2023

Document Version

Final published version

Published in

Fuel

Citation (APA)

Bao, H., Han, J., Zhang, Y., Di Matteo, A., Roekaerts, D., Van Oijen, J., & Somers, B. (2023). Large-eddy simulation of dual-fuel spray ignition at varying levels of methane diluted ambient oxidizer using FGM. *Fuel*, 351, Article 128901. <https://doi.org/10.1016/j.fuel.2023.128901>

Important note

To cite this publication, please use the final published version (if applicable).
Please check the document version above.

Copyright

Other than for strictly personal use, it is not permitted to download, forward or distribute the text or part of it, without the consent of the author(s) and/or copyright holder(s), unless the work is under an open content license such as Creative Commons.

Takedown policy

Please contact us and provide details if you believe this document breaches copyrights.
We will remove access to the work immediately and investigate your claim.



Full length article

Large-eddy simulation of dual-fuel spray ignition at varying levels of methane diluted ambient oxidizer using FGM

Hesheng Bao^{a,*}, Jinlin Han^a, Yan Zhang^{b,c}, Andrea Di Matteo^a, Dirk Roekaerts^d, Jeroen Van Oijen^a, Bart Somers^a

^a Department of Mechanical Engineering, Eindhoven University of Technology, Netherlands

^b CAEP Software Center for High Performance Numerical Simulation, China

^c Institute of Applied Physics and Computational Mathematics, China

^d Department of Process & Energy, Delft University of Technology, Netherlands

ARTICLE INFO

Keywords:

Engine Combustion Network
Spray A
Large-eddy simulation
Dual-fuel ignition
FGM
Ambient methane concentration

ABSTRACT

In the current work, the Flamelet Generated Manifold (FGM) method is applied with large-eddy simulation (LES) to investigate the effect of methane on dual-fuel (DF) spray ignition. The diesel surrogate *n*-dodecane is injected as the so-called pilot fuel into selected lean methane–air mixtures, ranging from $\phi_{\text{CH}_4} = 0$ to $\phi_{\text{CH}_4} = 0.75$, at engine relevant conditions. The operating conditions are those of the completely characterized Engine Combustion Network (ECN) Spray A configuration, for which the modeling approach adopted in the present study was extensively validated. The specific purpose of this study is to extend and validate the FGM approach for dual-fuel combustion. In order to understand the interplay of chemistry and mixing, the ignition behavior of selected cases is investigated. It is found that both low and high temperature combustion (LTC and HTC, respectively) are increasingly retarded by higher values of ϕ_{CH_4} , while the induction time between LTC and HTC is relatively insensitive compared to the ignition delay time (IDT). Analysis reveals a more prominent role of mixing for increased ϕ_{CH_4} . The development of LTC and HTC are quantitatively analyzed for different cases. The transition from LTC to HTC is found to be highly correlated with the evolution of lift-off length (LOL), which on its turn is seriously affected by ϕ_{CH_4} . The local flame behavior is analyzed via chemical explosive mode analysis (CEMA), suggesting a clear flame propagation due to diffusion towards lean mixtures after the ignition of the pilot fuel. Besides, it is found that diffusion helps to stabilize the flame in leaner mixtures, which is more important in DF combustion. The results show FGM to be a promising tool in modeling the DF sprays.

1. Introduction

The increasing public concern on sustainable development not only is leading worldwide to more stringent emission regulations for engines but also requires a reduced consumption of fossil resources. In order to contribute to achieving these requirements modern combustion engines must be designed to simultaneously achieve low emissions and high efficiency. Low-temperature combustion (LTC) concepts are of interest for achieving low emissions since they operate at lower cylinder temperature and fuel-lean conditions [1,2]. Among these LTC concepts, dual-fuel (DF) is combining the benefits of spark ignition (SI) and compression ignition (CI) engines. In a typical DF engines high-reactivity fuel is directly injected (DI) into the cylinder during the late compression stroke, in which a mixture of low-reactivity primary fuel and air is prepared by introducing the primary fuel via port

fuel injection (PFI) during the intake stroke. In this way, DI fuel and the premixed lean PFI fuel stratifies in terms of both reactivity and equivalence ratio [3]. For the reliability at different loads, various injection and valve scenarios are adopted to achieve desired in-cylinder fuel stratification, depending on engine configurations [4–6].

Predominantly made up of methane, natural gas is widely applied in combination with liquid fuel in DF engines because of its wide availability and clean combustion (lower CO₂ and almost no PM [7]). Moreover, the high octane number of methane results in high resistance for auto-ignition, allowing for higher compression ratios and thus higher thermal efficiency. A variety of experimental investigations have been carried out on DF engines, mainly concerning global engine performance and emissions. It is found that the premixed methane retards the auto-ignition of the diesel spray, and may result in combustion instabilities. Then misfire and higher unburnt hydrocarbons

* Corresponding author.

E-mail address: h.bao@tue.nl (H. Bao).

<https://doi.org/10.1016/j.fuel.2023.128901>

Received 16 March 2023; Received in revised form 30 May 2023; Accepted 2 June 2023

Available online 14 June 2023

0016-2361/© 2023 The Author(s). Published by Elsevier Ltd. This is an open access article under the CC BY license (<http://creativecommons.org/licenses/by/4.0/>).

(UHC) emissions due to incomplete combustion can result leading to a reduced thermal efficiency. A brief overview of experimental research regarding the influence of engine operating and design parameters on combustion characteristics is given in Ref. [8]. It is clear that more detailed understanding of the interactions between methane and diesel pilot spray and the subsequent flame initiation in DF applications may help to realize a stable combustion process.

Recently, optical techniques have been applied to explore the fundamental DF ignition mechanism in detail. By tracing the flame luminosity, Dronniou et al. concluded that the ignition preferably initializes in pilot fuel rich mixtures. It is pointed out that the equivalence ratio of the premixed in-cylinder mixture is a dominant factor for DF engines in terms of methane consumption and heat release by the direct influence on the flame propagation. It was pointed out that for all equivalence ratios, the flame propagation is observed to initialize at multiple sites near the wall and develop towards the central region within the piston bowl [9]. Similar observations can also be found in [10–12]. In other investigations, the sensitivity of intake air temperature and injection strategy on DF engine combustion characteristics was also explored [11, 13–15].

Schlatter et al. carried out a series of investigations on DF ignition using a rapid compression machine (RCM) [16–18]. A clear flame propagation in the ambient premixed mixture was observed for higher methane equivalence ratio, while a sustainable increasing chemiluminescence intensity was found in the vicinity of the pilot spray even for very lean premixed charge [16]. A quantitative study of OH* chemiluminescence and Schlieren imaging revealed a linear retarding effect of ambient methane equivalence ratio on ignition delay time (IDT) [18]. This trend was experimentally confirmed by Srna et al. in an RCM study [19,20]. In particular, the retarding effect was found to be strengthened at a higher methane equivalence ratio, which is similar to the effect of a reduced ambient temperature. To be precise, almost 80% of the prolonged IDT is attributed to the delay of first-stage ignition motivated by studying the formaldehyde fluorescence as an indicator for the low temperature ignition [21].

The ignition of DF combustion is observed to experience two phases, which is similar to the observation in conventional single-fuel (SF) diesel spray [22]. However, in the DF mode, two peaks of heat release rate exist, which are respectively attributed to ignition of the pilot spray with surrounding methane/air mixture and premixed flame propagation [18]. While the retarding effect of methane on DF ignition is well identified at varying conditions [23–26], the understanding of the corresponding flame development needs more efforts. Srna et al. investigated the transition from the pilot-fuel ignition to the premixed flame propagation by analyzing the heat release rate [19]. The underlying interactions between auto-ignition and flame propagation were addressed via species and radical analysis by means of advanced optical diagnostics [20]. It is noted that experimental investigations on DF combustion so far have only been made in engine and RCM configurations and only a limited number of numerical investigations concerning this combustion mode are available [27–29]. More investigations are needed regarding the local flame behavior in DF combustion, especially ignition.

As the scope of experimental data is relatively limited with respect to spray ignition, numerical research with adequate fidelity is needed to explore fundamental phenomena in DF combustion. Large-eddy simulation (LES) is an applicable and precise tool for turbulent igniting spray simulation. However, its relatively high computational cost, especially when integrating the chemistry directly and the subsequent higher mesh resolution required for resolving the flame structures makes it a challenge. The flamelet concept is a modeling approach in which the turbulent flame is regarded as an ensemble of local laminar flames (flamelets) [30] resulting in only a reduced number of transport equations to be solved, reducing the computational cost. Nevertheless, a large fraction of the existing numerical investigations regarding DF

sprays use the framework of direct chemistry integration and often neglect the subgrid turbulence–chemistry interaction (TCI) [23,26,29,31], despite the fact that TCI is of great importance for predicting the flame structure [32,33]. Although applying an advanced tabulated chemistry approach is more efficient, only a limited number of investigations can be found for DF ignition [34–36]. The Flamelet Generated Manifold (FGM) [37] as a typical tabulated flamelet approach, pre-tabulates and retrieves flamelet information according to several independent controlling variables. In FGM, the set of flamelet governing equations is derived from the full set of in-stationary three-dimensional conservation equations and are solved in physical space [38]. Although FGM was shown to be promising in predicting the ignition behavior in engines [39,40], it is not yet validated in detail in the flamelet framework and applied in a DF combustion mode. This paper first validates the application of the FGM approach to DF combustion by comparison with detailed chemistry results in laminar flamelet calculation. Next, the performance of the FGM in an LES application is first validated by comparison of model predictions with experimental data for the SF spray and then further applied to DF sprays.

The Engine Combustion Network (ECN) [41] establishes an international collaborative experimental and numerical research, allowing extensive characterization of the spray ignition process for validating computational models. The present study is made for the ECN Spray A baseline condition but is extending them to dual fuel cases. It has been found earlier that the molar ratio of methane and *n*-dodecane is the key issue affecting the ignition characteristics [42]. Therefore to investigate the effect of methane on the DF ignition process, in this study different amounts of methane are added to the ambient oxidizer of Spray A, keeping the oxygen mole fraction constant. In practice these cases cannot be realized experimentally in the ECN configuration (the methane would decompose and start burning during mixture preparation at high pressure and temperature). Therefore detailed validation of model predictions is not possible. Nevertheless, the base case predictions (single fuel) are validated comprehensively. This article aims to investigate DF sprays within a numerical framework. Following our previously presented modeling approach [43,44], the main objectives of the present research are: (1) to validate the application of FGM on DF combustion prediction, (2) to explore the flame development and characteristics of DF spray combustion, (3) to quantitatively define the effect of methane on *n*-dodecane spray ignition and the subsequent interactions between turbulent mixing and chemistry, and (4) to explore the corresponding local flame modes using Chemical explosive mode analysis (CEMA) [45].

The present paper is structured as follows. The numerical methods and related models are described in Section 2, followed by a detailed description on case and computational setup in Section 3. In Section 4, the chosen cases are investigated within the framework of various dimensional simulations. The effect of ambient methane on turbulent spray ignition is analyzed in detail in conjunction with the lower-dimensional simulations. Finally, a summary of findings are given in Section 5.

2. Numerical methods

2.1. Gaseous phase governing equations

In the present study, the turbulent gaseous phase flow is described by LES equations. Any variable ϕ is decomposed into a density weighted filtered part $\bar{\phi}$ and a fluctuation ϕ'' . A Favre filtered value is defined by a spatial-filtering operation via the Reynolds filter value: $\tilde{\phi} = \bar{\rho}\phi/\bar{\rho}$. The filtered conservation equations for mass, momentum, and energy read:

$$\frac{\partial \bar{\rho}}{\partial t} + \frac{\partial \bar{\rho} \tilde{u}_i}{\partial x_i} = \tilde{S}_\rho, \quad (1)$$

$$\frac{\partial \bar{\rho} \tilde{u}_i}{\partial t} + \frac{\partial \bar{\rho} \tilde{u}_i \tilde{u}_j}{\partial x_j} = -\frac{\partial \bar{p}}{\partial x_i} + \bar{\rho} g + \frac{\partial \bar{\tau}_{ij}}{\partial x_j} - \frac{\partial \bar{\rho} \tilde{\Gamma}_{ij}}{\partial x_j} + \tilde{S}_{u,i}. \quad (2)$$

ρ , u_i , p , τ_{ij} represent the fluid density, velocity, pressure and viscous stress tensor, respectively. \bar{F}_{ij} is the turbulent stress tensor that needs to be modeled. In this investigation, \bar{F}_{ij} is treated as a non-viscosity shear stress that is calculated by a dynamic structure (DS) model [46]. This model solves an additional subgrid kinetic energy transport equation. In addition, a correction factor is applied in the region with local high strain rate near the nozzle. For more details, we refer to Ref. [47]. The coupling between liquid and gaseous phases is realized through source terms \bar{S}_ρ , $\bar{S}_{u,i}$, and \bar{S}_h . It is noted that in FGM, species mass fractions, and also temperature, are directly retrieved from the prepared database.

2.2. Spray modeling

The Discrete Droplets Model (DDM) is applied for solving the discrete liquid phase. A so-called “face-to-face” algorithm is adopted for parcel tracking [48]. The spherical drag model is used for describing the momentum exchange between gaseous flow and liquid droplets [49]. A LES-specific dispersion modeling approach is implemented to describe in statistical manner the influence of the relative velocity between the gas and droplets [44,50]. Collisions between droplets are included such that a “four-way coupling” is enabled [51]. The mass and heat transfer between the gaseous flow and droplets at the interface is modeled following literature [52,53]. The fuel distribution after the primary breakup is given by the Rosin-Rammler size distribution, followed by a secondary breakup that is modeled by the Kelvin–Helmholtz and Rayleigh–Taylor (KH-RT) instabilities [54]. The modeling approach was described and extensively validated in our previous investigation. More details can be found in Ref. [44].

2.3. Numerical schemes

The finite-volume method is used to solve the gaseous phase governing equations. The time integration adopts an implicit second-order backward differencing scheme. Adjustable time-stepping is allowed by evaluating the Courant–Friedrichs–Lewy (CFL) number (set to 0.3 in this study). All Laplacian schemes are discretized by a second-order linear central differencing scheme, while the convective terms apply a blend of first- and second-order scheme considering the computational cost. For the pressure–velocity coupling, the PISO (Pressure-Implicit with Splitting of Operators) corrector is chosen. The modeling approach is implemented within the open-source CFD package – OpenFOAM.

2.4. Combustion modeling

The combustion modeling approach adopted in this study is FGM. It is a combination of flamelet model and chemistry reduction approach exploiting that the result of chemical reactions and diffusion in a high-dimensional composition space can be reduced to evolution on a low-dimensional manifold that can be calculated from a set of laminar flames. The manifold is constructed using results of simulations of representative laminar counterflow diffusion flames (flamelets) using detailed chemistry. In this investigation, the flamelets are solved in physical space using CHEM1D [55]. In this paper, four cases are studied as listed in Table 1. For SF simulation, the flamelet boundary conditions for fuel and oxidizer are set as the ECN Spray A experiments. For DF cases, it is assumed that the ambient gas for each case is homogeneously mixed and each represents a dilution level. Thus, the typical stratifications in DF engines are not considered, and oxidizer boundary conditions for flamelet simulation are set individually for different cases. However, the stratifications as results of mixing between the pilot fuel and a certain methane/air mixture are included. The commonly adopted Yao et al. mechanism (54 species and 269 reactions) [56] when simulating the *n*-dodecane flames is applied. The feasibility of using Yao et al.’s mechanism in predicting methane/*n*-dodecane DF combustion was justified by Kahila et al. [57]. The methane-specific

part was validated for both IDT given by homogeneous reactors and flame speed and structure by flamelet calculations against the well-known GRI-3.0 [58] mechanism. Besides, it was proven that the most sensitive reactions in the DF cases are mostly the same as that in the SF case, and the ambient methane mainly affects the early decomposition of *n*-dodecane, which is captured by the Yao et al.’s mechanism. This motivates the use of Yao et al.’s mechanism for both SF and DF cases in this work. FGM parameterizes the full set of flamelet solutions as function of a reduced number of controlling variables. An FGM that takes the scalar dissipation rate, χ , into account is applied [43]. χ is directly dependent on the strain rate applied on the boundary of the counterflow diffusion flame configuration. It is thus included as an additional parameter to characterize the state of each flamelet. Including χ in FGM was previously shown to significantly affect the species formation and transition of LTC to HTC in rich-mixtures [43]. The other two controlling variables are mixture fraction Z and reaction progress variable Y_c . Z is an indicator of local fuel equivalence ratio. Bilger’s definition is used to determine its value locally in the flamelets [59]. the progress value Y_c takes different values when a transient igniting flamelet evolves from the unburnt mixing state and to the final steady state. It is typically defined as a linear combination of several representative species. The chosen combination has a set of values uniquely corresponding to different states of reaction. In this investigation, the progress variable is optimized and defined following Vasavan et al. [60]. A multi-objective optimization approach is applied to find a reaction progress variable that well fits the igniting flamelets. The optimized progress variable definition makes sure that ignition behavior at different applied strain rates can be accurately predicted through retrieval. Details of the optimized combination are listed in Table A.2. A top-hat filtering PDF is applied to the mixture fraction to account for the effect of turbulence fluctuations on chemical reactions [61]. To obtain the controlling variables discussed above in turbulence, governing equations of \tilde{Z} and \tilde{Y}_c must be included:

$$\frac{\partial \tilde{\rho} \tilde{Z}}{\partial t} + \frac{\partial \tilde{\rho} \tilde{u}_j \tilde{Z}}{\partial x_j} = \frac{\partial}{\partial x_j} \left[\tilde{\rho} \left(\frac{\nu}{Sc} + \frac{\nu_{sgs}}{Sc_{sgs}} \right) \frac{\partial \tilde{\rho} \tilde{Z}}{\partial x_j} \right] + \tilde{S}_Z, \quad (3)$$

$$\frac{\partial \tilde{\rho} \tilde{Y}_c}{\partial t} + \frac{\partial \tilde{\rho} \tilde{u}_j \tilde{Y}_c}{\partial x_j} = \frac{\partial}{\partial x_j} \left[\tilde{\rho} \left(\frac{\nu}{Sc} + \frac{\nu_{sgs}}{Sc_{sgs}} \right) \frac{\partial \tilde{\rho} \tilde{Y}_c}{\partial x_j} \right] + \tilde{\omega}_{Y_c}. \quad (4)$$

ν and Sc respectively denote the kinematic viscosity and Schmidt number, while the subscript sgs refers to the subgrid scale. \tilde{S}_Z is the source term due to evaporation, which is related to \tilde{S}_ρ which appeared in Eq. (1). $\tilde{\omega}_{Y_c}$ refers to the source term of the reaction progress variable and is retrieved from the FGM database.

To construct the top-hat PDF, the variance of \tilde{Z} , is obtained from the following equation:

$$\frac{\partial \tilde{\rho} \tilde{Z}_v}{\partial t} + \frac{\partial \tilde{\rho} \tilde{u}_j \tilde{Z}_v}{\partial x_j} = \frac{\partial}{\partial x_j} \left[\tilde{\rho} \left(\frac{\nu}{Sc} + \frac{\nu_{sgs}}{Sc_{sgs}} \right) \frac{\partial \tilde{\rho} \tilde{Z}_v}{\partial x_j} \right] + 2 \tilde{\rho} \left(\frac{\nu}{Sc} + \frac{\nu_{sgs}}{Sc_{sgs}} \right) \left| \frac{\partial \tilde{Z}}{\partial x_j} \right|^2 - 2 \tilde{\rho} \tilde{\chi}. \quad (5)$$

The quantity $\tilde{\chi}$ is the scalar dissipation rate acting as a sink term in the \tilde{Z}_v equation. Physically, it describes the effect of mixing leading to flattening of the gradients of mixture fraction. It can be decomposed into an explicit resolved part and a subgrid part that needs to be modeled:

$$\tilde{\rho} \tilde{\chi} = \tilde{\rho} \tilde{\chi}_{res} + \tilde{\rho} \tilde{\chi}_{sgs}, \quad (6)$$

where $\tilde{\chi}_{res} = \nu / Sc |\nabla \tilde{Z}|^2$, and $\tilde{\chi}_{sgs} = \nu_{sgs} / Sc_{sgs} / \Delta^2 \tilde{Z}_v$ [62]. More details regarding retrieval algorithms and the top-hat filtering PDF can be found in Ref. [43,44].

2.5. Flame identification

Different flame propagation modes exist in the reaction zones and are rather relevant to the flame stabilization. Computational Singular Perturbation (CSP) theory systematically identifies timescales and

reaction modes of complex detailed chemical kinetics [63]. CSP has been widely incorporated in the analysis of combustion processes [64]. Chemical explosive mode analysis (CEMA) is a computational diagnostic tool for identifying specific combustion modes in a flame [65], and has been extensively applied in study of auto-ignition in turbulent combustion. Both methods are based on eigenvalue analysis of the chemical Jacobian \mathbf{J} , a matrix built from the partial derivatives of the source terms with respect to the value of the reacting variables. The Jacobian determines in a linear approximation the growth or decay of the system:

$$\frac{D\omega(\mathbf{y})}{Dt} = \frac{\partial \omega}{\partial \mathbf{y}} \frac{D\mathbf{y}}{Dt} = \mathbf{J} \cdot \frac{D\mathbf{y}}{Dt} = \mathbf{J}(\omega + s), \quad (7)$$

where D/Dt is the material derivative. \mathbf{y} is the vector of local reacting variables, containing temperature and species mass fractions. ω denotes the chemical source term, and s includes the non-chemical source terms, such as the diffusion. This linear system has eigenvalues λ_e with corresponding eigenvectors. Each eigenvalue defines a mode. λ_e and \mathbf{J} are related via:

$$\lambda_e = \mathbf{b}_e \cdot \mathbf{J} \cdot \mathbf{a}_e, \quad (8)$$

where \mathbf{b}_e and \mathbf{a}_e are the left and the right eigenvectors, respectively, corresponding to λ_e . A mode is called explosive if the real part of the corresponding eigenvalue λ_e is positive. Such mode is observed in the pre-ignition zone, indicating the propensity of ignition (rapid growth) in isolated mixture [45]. On the contrary, a negative λ_e indicates the evolution towards chemical equilibrium, as occurring in the mixtures in the final phase after ignition has taken place. But it is worth mentioning that so-called cool flames occurring as initial phase of combustion for fuel with long hydrocarbons may also experience negative λ_e . Following literature [66], a temperature criterion, $T > 1100$ K, is applied to characterize only the mixtures in late combustion stage. Eigenvalue $\lambda_e \ll 1$ and local equivalence ratio $\phi < 0.01$ identify chemically inactive mixtures.

The Jacobian is obtained from the source term, but whether or not a system shows growth or decay depends on the combination of the effects reaction and diffusion. To identify what happens under the influence of a mode with positive eigenvalue (CEM), the relative strength of both effects needs to be compared [67]. To do so, both the change by chemistry and by diffusion in Eq. (7) are projected on the considered mode:

$$\mathbf{b}_e \cdot \frac{D\omega(\mathbf{y})}{Dt} = \mathbf{b}_e \cdot \mathbf{J}(\omega + s) = \lambda_e \mathbf{b}_e \cdot (\omega + s), \quad (9a)$$

$$\frac{D\phi_\omega}{Dt} = \lambda_e \phi_\omega + \lambda_e \phi_s + \frac{D\mathbf{b}_e}{Dt} \cdot \omega(\mathbf{y}). \quad (9b)$$

$\phi_\omega \equiv \mathbf{b}_e \cdot \omega$ and $\phi_s \equiv \mathbf{b}_e \cdot s$ are projected chemical and diffusion source terms, respectively. The last term in Eq. (9b) accounts for the rotation of the eigenvector. The local effect of the mode is evaluated via an indicator, α , following:

$$\alpha = \phi_s / \phi_\omega. \quad (10)$$

Consequently, the relative domination of chemistry and diffusion within the pre-ignition mixtures can be quantitatively identified following (i) $\alpha > 1$: assisted-ignition mode in which local ignition is promoted by diffusion, (ii) $|\alpha| < 1$: auto-ignition mode where chemistry plays a more primary role than diffusion, and (iii) $\alpha < -1$: so called “extinction” mode that diffusion and heat loss impede the ignition process. It is noted that “extinction” here refers to the local dynamical tendency to extinguish rather than a global extinction process. This mode only exists with strong local mixing. More detailed explanations on the flame modes can be found in literature [68].

3. Case description

The benchmark ECN case, Spray A [69], is taken as the experimental reference in this investigation. *n*-dodecane as the diesel surrogate is injected into a combustion chamber in which the ambient is meticulously

Table 1

Specifications for the cases studied.

Parameter	ECN Spray A	DF1	DF2	DF3
Injection conditions				
Fuel		<i>n</i> -dodecane		
Nominal nozzle diameter [μm]		90		
Fuel temperature [K]		363 (155)		
Injection pressure [MPa]		150		
Injection duration [ms]	∞	∞	∞	∞
Ambient conditions				
Ambient temperature [K]	900			
Ambient pressure [MPa]	6			
ϕ_{CH_4} [-]	0	0.25	0.50	0.75
O ₂ molar fraction [-]	0.1500			
N ₂ molar fraction [-]	0.7515	0.7349	0.7184	0.7018
CO ₂ molar fraction [-]	0.0623	0.0609	0.0596	0.0582
H ₂ O molar fraction [-]	0.0362	0.0354	0.0346	0.0338
CH ₄ molar fraction [-]	0	0.0188	0.0375	0.0563
Density [kg/m ³]	23.4	23.3	23.1	22.9
Z_{st} [-]	0.0451	0.0345	0.0234	0.0120

well defined following the typical conditions in diesel engines. For both mixing and reacting characteristics, an extensive database is available in a variety of fuel and ambient conditions [41]. In this investigation, the standard Spray A configuration is chosen as the baseline. The DF cases are then derived from the baseline case by adding methane to the ambient. Following the work by Kahila et al. [24], the molar fraction of oxygen is kept the same and in the rest of the mixture methane is increased while the other components are reduced keeping their relative proportions fixed. In such a way, the density of the ambient gas is preserved. Cases with different equivalence ratios of the methane/oxygen mixture are investigated. In Table 1, details of the case configurations are summarized. It is noted that only experiments for the standard ECN Spray A are available. The methane equivalence ratio of the ambient is denoted by ϕ_{CH_4} . Z_{st} represents the stoichiometric mixture fraction calculated taking *n*-dodecane as fuel and the ambient mixture, including the methane, as oxidizer. For the cases studied, the density of the DF ambient mixtures varies 2.5% at most compared to the benchmark ECN case.

4. Results

In this section, the influence of ambient methane equivalence ratio (ϕ_{CH_4}) on *n*-dodecane reacting spray is investigated considering the cases specified in Table 1. The simulation results are organized in the following order: homogeneous reactor simulations, counterflow diffusion flame, and LES spray combustion. Following [70], all simulations are based on the lowered fuel temperature (155 K) assumption compared to the nominal fuel temperature specified in Table 1. In this way, the enthalpy change due to fuel evaporation is taken into account. The resulting adiabatic mixing line can be found in [44]. According to the available literature, it is confirmed both experimentally [18,21,22] and numerically [24,40,57] that the development of both SF and DF go through three different phases, (1) turbulent mixing that is prior to the ignition, (2) the initialization of first-stage combustion, i.e. the low temperature combustion (LTC), and (3) the initialization of second-stage combustion, i.e. the high temperature combustion (HTC). In this investigation, the attention is drawn to the two stages of combustion and specifically to the differences induced by the addition of methane in the ambient.

4.1. Homogeneous reactor simulation

Zero-dimensional constant pressure homogeneous reactor simulations were made using the open-source software Cantera [71]. Attention is paid to ignition behavior of mixtures lying on a modified

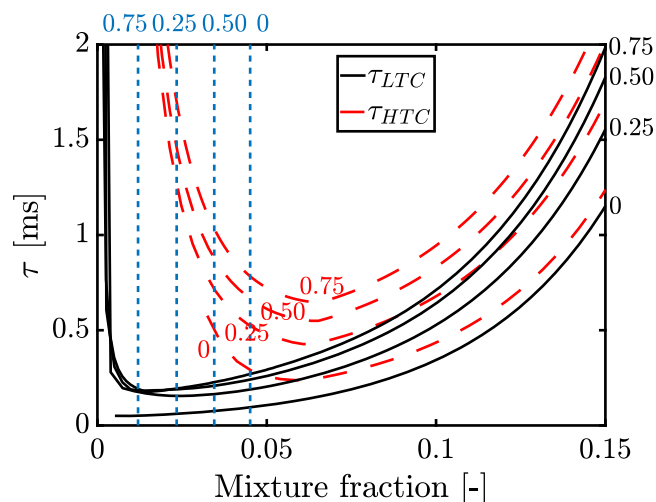


Fig. 1. τ_{LTC} and τ_{HTC} starting from the adiabatic mixing line including the evaporation for different methane equivalence ratios, calculated by constant pressure homogeneous reactors. The vertical dotted lines mark the stoichiometric mixture fraction for the different ϕ_{CH_4} .

adiabatic mixing line computed from a laminar counterflow configuration. Modified here refers to the fact that it is calculated based on a lowered fuel temperature as mentioned above. Every mixing state thus has a specific temperature depending on the mixture fraction, and is used to initialize a homogeneous reactor.

The decomposition of alkyl radicals is the prominent process corresponding to low temperature hydrocarbon oxidation. Thus, following Kahila et al. [57], the ignition of LTC is defined as the time instance when 20% of the maximum mass fraction of dodecyl peroxy radical, $C_{12}H_{25}O_2$ (RO_2), is observed. When approaching the second-stage ignition, H_2O_2 steadily accumulates, while its consumption is much slower than its production. OH is widely adopted as an indicator within the ECN framework to characterize the IDT. As an HTC product, OH was reported to highly correspond to the change of H_2O_2 . An intense increase of OH, followed by a rapid temperature rise, generally is started by a significant acceleration of H_2O_2 decomposition [72]. Accordingly, in this investigation the ignition of HTC is defined as the time instance when the maximum consumption rate of H_2O_2 ($\dot{\omega}_{H_2O_2,cons}$) occurs. Besides, the HTC is only considered as “activated” when the maximum mass fraction of H_2O_2 is greater than 2.5×10^{-4} , while a temperature of over 1150 K is taken as a characterization of HTC [73]. In the following, the ignition delay time of LTC and HTC are denoted by τ_{LTC} and τ_{HTC} , respectively. Consequently, the values of τ_{LTC} and τ_{HTC} along the adiabatic mixing line for different ambient methane levels are presented in Fig. 1. We recall that the notation IDT, defined differently from the τ_{HTC} , in this paper refers to the time when 2% of the maximum OH mass fraction is first seen during ignition. It is found that IDT is different from the τ_{HTC} .

It is noted that in SF configuration, the second-stage ignition does not happen for the fuel-lean mixtures and neither first- nor second-stage ignition happens for the very lean mixtures. However, due to the presence of methane in the oxidizer, first-stage ignition is achieved in relatively lean mixtures compared to that in the SF case. In the case of $\phi_{CH_4} = 0.5$ and $\phi_{CH_4} = 0.75$, HTC is seen even in the pure oxidizer. Nevertheless, τ_{LTC} is over 70 ms. It is much longer than typical engine cycle times. The IDT of Spray A configuration studied in this work is approximately 0.39 ms in experiment [74]. Therefore it is not necessary to include the auto-ignition of pure oxidizer in the FGM table. But this might not be universally the case. For applications with higher ambient pressure or temperature, whether to take the ignition of the oxidizer into account must be carefully evaluated.

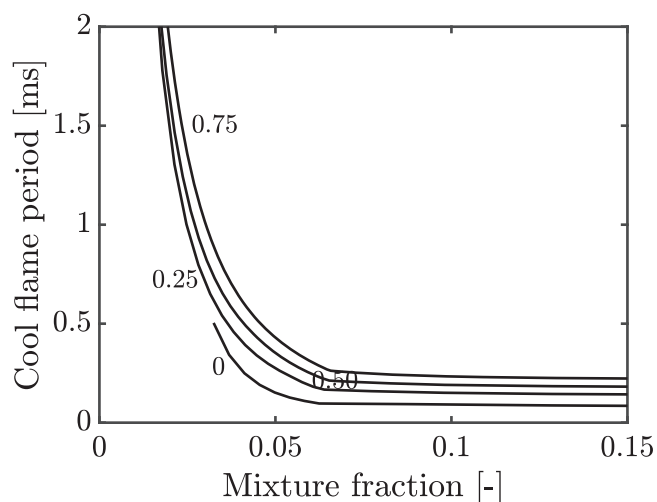


Fig. 2. Cool flame periods starting from the adiabatic mixing line for different methane equivalence ratios, calculated by constant pressure homogeneous reactors.

According to Fig. 1, apart from the very lean mixtures, both τ_{LTC} and the gradient of τ_{LTC} are observed to increase with an increase of mixture fraction in the range (0.05–0.15). Unlike τ_{LTC} , the tendency of τ_{HTC} is not monotonous in mixture fraction space. For each ϕ_{CH_4} case, a shortest τ_{HTC} , the so-called most reactive mixture fraction Z_{MR} [75], is observed. $Z_{MR,HTC}$ increases with ϕ_{CH_4} and appears at a richer mixture than the corresponding stoichiometric mixture fraction Z_{st} (listed in Table 1). At a specific mixture fraction, both τ_{LTC} and τ_{HTC} are retarded with an increased ϕ_{CH_4} as expected. This is consistent with the observation in experiments [18–20]. However, it must be stressed that in engine applications, the initialization of LTC highly depends on the turbulence level considering the weak reactivity in this stage. Hence the actual effect of ϕ_{CH_4} on LTC must be evaluated in higher dimensional flames.

Fig. 2 indicates the influence of ϕ_{CH_4} on the duration of the so-called cool flame period ($\tau_{HTC} - \tau_{LTC}$). It is seen that the value of the cool flame period reduces as mixture fraction increases until a relatively stable value is achieved. Especially for richer mixtures ($Z > Z_{MR,HTC}$), the change of the cool flame period due to ϕ_{CH_4} is very limited compared to the magnitude of τ_{HTC} . This may partially explain the observation in the RCM study that the inhibiting effect of methane mainly acts on the first-stage ignition [21]. For leaner mixtures, τ_{HTC} is too long compared to the duration of an engine cycle. In such a situation it is necessary to study the effect of ϕ_{CH_4} on the cool flame period further via a turbulent flow simulation.

4.2. Counterflow diffusion flame simulation

In this section, transient simulations of one-dimensional counterflow diffusion flame are carried out to investigate the role of mixing and diffusion on the retarding effect of ambient methane in the oxidizer within a laminar framework. First, laminar flames, including both SF and DF cases following Table 1, with detailed chemistry are investigated in terms of ignition behavior. To justify the FGM approach applied in the present paper, the results of DF flames using detailed chemistry are compared to the simulations using FGM with respect to a variety of parameters before its application to turbulent flows.

4.2.1. Results of detailed chemistry

The flamelet equations solved are based on the so-called strongly stretched flamelet equations formulated on the basis of the mass burning rate [76]. The change of mass flux perpendicular to the flow-axis is considered via the local stretch rate [38]. A transport equation is

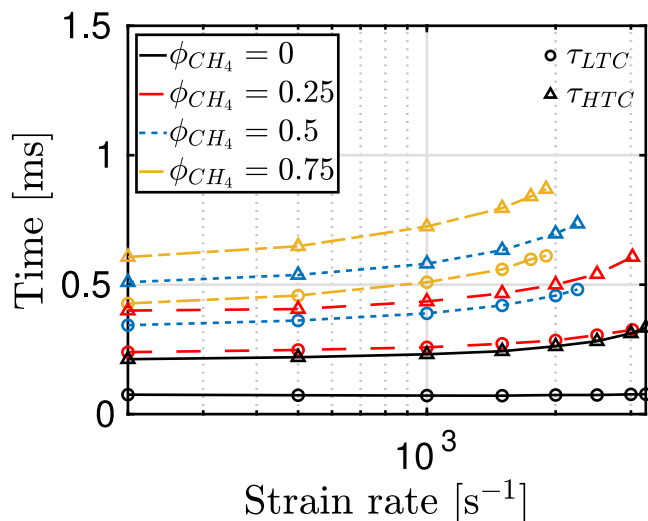


Fig. 3. Tendency of τ_{LTC} (marked by \circ) and τ_{HTC} (marked by Δ) on strain rate for different methane equivalence ratios (indicated by different line types in different colors), calculated from one-dimensional counterflow diffusion flame.

used to describe this stretch rate, where the strain rate a acts as the boundary condition that is prescribed in the oxidizer stream [77]. For clarification, the term strain rate in the following always refers to this applied strain rate as a parameter of the counterflow configuration. The strain rate directly influences the strength of flow effects on chemical processes, and changes the course of combustion. Thus, it is worthwhile to study the influence of ϕ_{CH_4} on igniting flamelets as a function of this strain rate.

Fig. 3 depicts the dependencies of τ_{LTC} and τ_{HTC} on the strain rate for different ϕ_{CH_4} . For consistency, τ_{LTC} and τ_{HTC} are defined using the same thresholds as in Section 4.1. It is noted that the maximum values are calculated from all mixture fractions, while in the case of homogeneous reactors, the maximum values refer to individual mixtures. For each ϕ_{CH_4} , only the igniting flamelets at strain rate lower than the ignition limit strain rate are analyzed and shown. It is seen that both the strain rate and ϕ_{CH_4} affect the ignition. For all ϕ_{CH_4} , the retarding effect of strain rate on τ_{HTC} is more significant than that on τ_{LTC} . For the SF case ($\phi_{CH_4} = 0$), τ_{LTC} is hardly influenced by the strain rate while a clear prolonged τ_{HTC} is observed as the strain rate increases. On the contrary, the effect of strain rate on τ_{LTC} is amplified as ϕ_{CH_4} increases. In DF cases, both τ_{LTC} and τ_{HTC} are retarded by an increased ϕ_{CH_4} . This is consistent with the results found using zero-dimensional homogeneous reactors.

A quantitative analysis of the effect of methane addition is presented in Fig. 4. In Fig. 4, the IDTs depicted by open symbols are shown as a reference. Here, the IDT is defined by the time when 2% of the maximum OH mass fraction during ignition is seen in the flamelet. It is obvious that the increase of ϕ_{CH_4} in the oxidizer results in a reduced ignition limit strain rate. Although both τ_{LTC} and τ_{HTC} are retarded by ϕ_{CH_4} according to Fig. 3 and also found in Fig. 1, it is clear that the cool flame period for various ϕ_{CH_4} remain almost constant for a specific strain rate compared to the magnitude of the corresponding IDT. In other words, the retarding effect of methane addition in oxidizer is mainly attributed to the prolonged first-stage ignition. This supports the statement in the experimental study [21]. Later, in the study of the turbulent flame the difference in ignition as a result of ϕ_{CH_4} will be found to have a direct effect on the LOL. Besides, the relatively constant cool flame period is similar to the observation in homogeneous reactors for the fuel-rich mixtures in Section 4.1. This illustrates that the chemical retarding effects of ϕ_{CH_4} in the fuel-lean mixtures are not as prominent as those in the fuel-rich mixtures due to the mixing and diffusion.

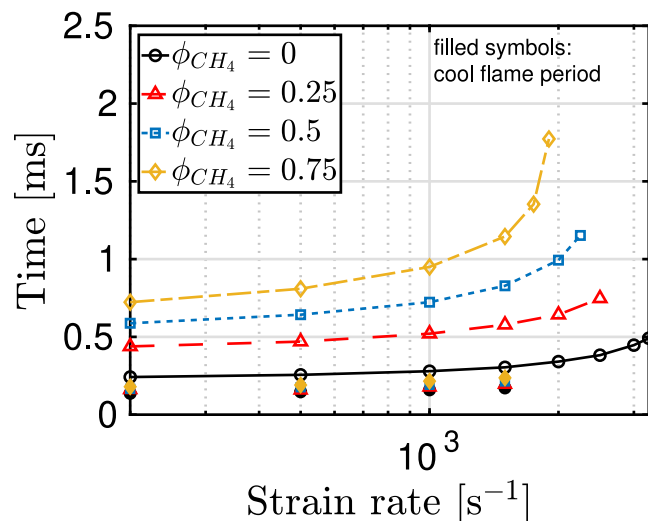


Fig. 4. Tendency of IDT (marked by lines with open symbols) and cool flame period (marked by filled symbols) as function of strain rate for different methane equivalence ratios (indicated by different line types in different colors), calculated from one-dimensional counterflow diffusion flame.

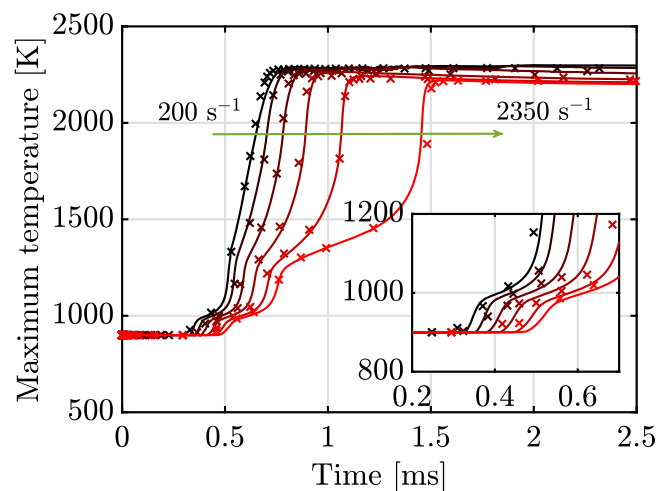


Fig. 5. Performance of FGM in predicting the dual-fuel ignition ($\phi_{CH_4}=0.5$). Lines: prediction of detailed chemistry. Crosses: prediction of FGM.

4.2.2. Performance of FGM in predicting the dual-fuel combustion

In this section, the performance of the FGM on capturing the DF flame is validated in terms of ignition, species and velocity of a “pre-mixed” flame front. All simulations are carried out within the framework of a one-dimensional laminar flame. The $\phi_{CH_4}=0.5$ case (DF2) is chosen in the following as an example.

The FGM applied for turbulent combustion simulation in this investigation takes the effect of scalar dissipation rate into account. The evolution of scalar dissipation rate for each igniting flamelet is stored in the database and used as an additional controlling variable for retrieval. Following [43], the procedure is to find the applicable strain rate a for prevailing Z , Y_c , and χ as part of the lookup in the FGM table. Thus, before proceeding to more complex applications it is important to first evaluate the accuracy of FGM when it is used to calculate the flame evolution of igniting counterflow flamelets for a wide range of applied strain rates. In Fig. 5, the evolution of maximum temperature shown illustrates that the ignition process at all strain rates is well captured by FGM. With an increased strain rate value, the detailed chemistry results show a reduced maximum temperature as well as a retarded ignition as expected. This phenomenon is well described by FGM. Also, the three

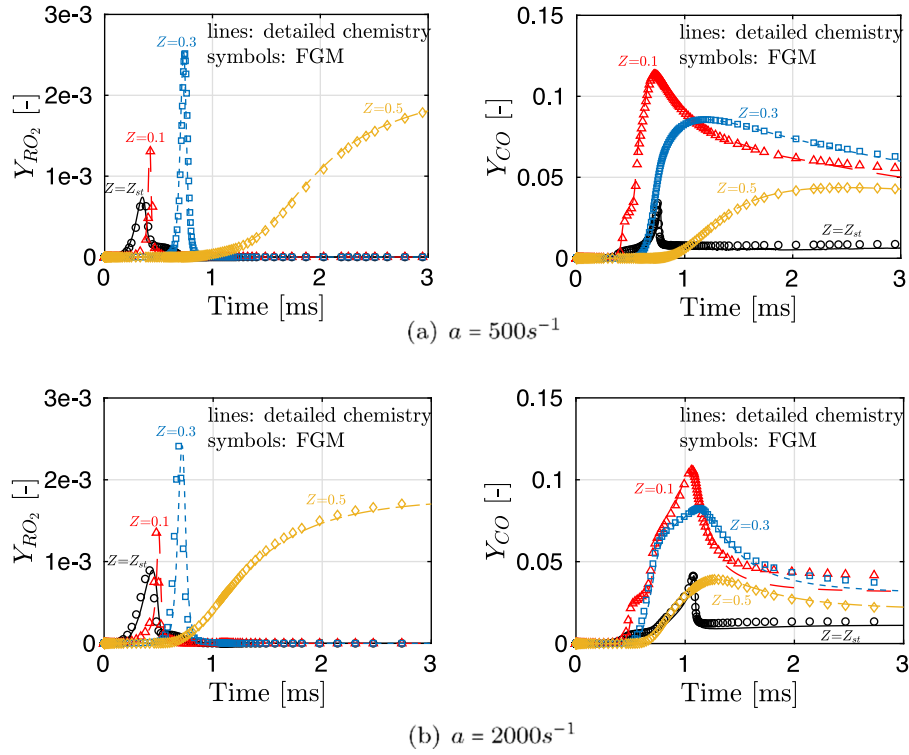


Fig. 6. Performance of FGM in predicting species formation. ($\phi_{\text{CH}_4}=0.5$)

phases of maximum temperature evolution for the DF ignition are well reproduced by the FGM.

Fig. 6 depicts the comparison of FGM and detailed chemistry at $a=500 \text{ s}^{-1}$ and at $a=2000 \text{ s}^{-1}$ as example. RO_2 and CO as the representative species for LTC and HTC are studied. For visibility, the mass fraction of RO_2 at Z_{st} is multiplied by a factor of 10. FGM provides excellent agreement to the detailed chemistry regarding developments of both RO_2 and CO . The variation of species formation due to strain rate applied is also well captured.

CHEM1D calculates a flamelet in physical space using a canonical counterflow configuration to represent the flamelet in the current application. The ignition initializes in the vicinity of Z_{MR} and propagates to the surroundings. In the DF combustion mode, the counterflow flame is defined by a premixed methane–air mixture at one side and a pure fuel (*n*-dodecane) on the other side. The flame is thus not purely non-premixed. It is of interest to evaluate the performance of FGM on capturing the flame propagation of the flame front towards the premixed fuel steam. Here, the position closest to the fuel stream where the gradient of flow velocity is zero is evaluated. In Fig. 7, the performance of FGM on capturing the flow velocity and temperature is shown for the quasi-steady state. It is seen that the flame calculated by FGM provides a good agreement to the detailed chemistry in physical space. The position closest to the fuel stream where the gradient of the flow velocity is zero is excellently predicted by FGM.

The investigation shows that FGM predicts the ignition behavior as well as the propagation of the premixed flame in a DF application.

4.3. Large-eddy simulation

In this section, results of large-eddy simulations of SF spray and DF sprays derived from ECN Spray A condition [41] are analyzed. The non-reacting spray predicted by the currently adopted modeling approach was introduced and extensively validated in our previous study [44]. In the present investigation, this modeling approach is directly applied in DF cases. After a brief description of the setup the result are analyzed from different points of view: global detailed

evolution of spray flame in physical space, evolution in mixture fraction space, and finally combustion mode analysis (CEMA).

4.3.1. Configuration

The computational domain is a cylinder with a diameter of 47 mm to simulate the part of the combustion chamber, in which the flame develops. The domain is discretized into a structured hexahedral mesh. A refinement around the spray axis in the core region is applied in order to better describe the spray development. The injector is located on the base of the mesh. The other part of the mesh has expansion ratios of 1.015 and 1.01 for radial and axial directions, respectively. The base grid size is set as $62.5 \mu\text{m}$ as suggested by literature [78]. This leads to a total number of 3.6 million cells. This mesh has been successfully applied and its quality is extensively validated within the framework of the ECN Spray A configuration. Details regarding the currently adopted mesh can be found in [79]. Using the numerical approaches applied in the current paper, this mesh was proven to perform well for both the inert [44] and reacting Spray A configuration [43].

4.3.2. Global view: ignition and flame stabilization

This section provides an overall impression on ignition and flame stabilization, the lift-off length (LOL), with varying ambient methane concentrations. As mentioned, auto-ignition processes of both SF and DF configuration are characterized by initialization of LTC and HTC. For consistency, the values for τ_{LTC} and τ_{HTC} in a turbulent system are defined in the same way as in the homogeneous reactor (Section 4.1) and counterflow diffusion flame (Section 4.2) and are based on the LES-filtered values. In our previous work, the influence of injection-to-injection variation on global combustion parameters were studied. It was proven that a single LES realization is sufficient for IDT and LOL by evaluating the I_{xt} -integrals [44]. As is employed by Maes et al. [80], the radially integrated intensity of a species i at time t is defined by:

$$I_{xt,i}(x, t) = \int \tilde{Y}_i(x, y, z, t) dy dz, \quad (11)$$

where x and y refer to the axial distance from the nozzle orifice and the radial distance from the spray axis, respectively. In this study, the

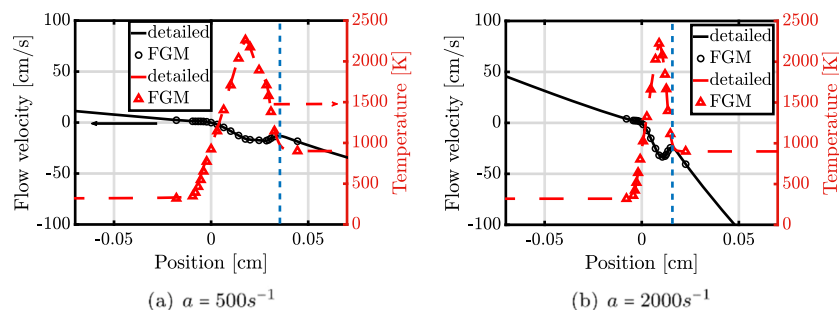


Fig. 7. Performance of FGM in predicting flow velocity and temperature, the dotted blue lines indicate the stabilization point of the zero-gradient flow velocity that is closest to the fuel stream predicted by the detailed simulation. ($\phi_{CH_4}=0.5$, quasi-steady state).

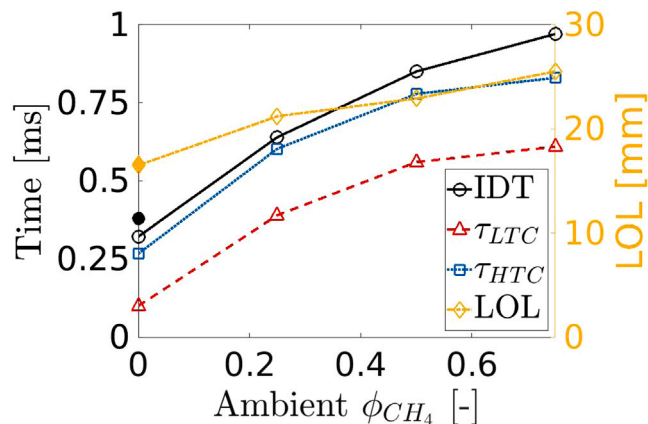


Fig. 8. Influence of ambient methane equivalence ratio ϕ_{CH_4} on global combustion parameters. Experimental IDT and LOL for standard Spray A ($\phi_{CH_4} = 0$) [69] are marked by filled symbols.

intensity of a species corresponds to its mass fraction, and is used to evaluate the IDT and LOL. The IDT is defined as the time when 2% of the maximum $I_{x,OH}$ in the system is reached. This OH-based IDT definition is chosen following the suggestions given by [24,57]. The LOL is defined as the smallest x in the domain where the condition $I_{x,OH} \geq 2\%$ of maximum $I_{x,OH}$ is satisfied. A time-averaged LOL for the quasi-steady state from 1.5 ms to 2 ms is used to compare to the ECN experiments [41].

Fig. 8 shows the simulated IDTs and LOLs as function of ϕ_{CH_4} . As comparison, the experimental values for standard Spray A (the SF case) [69] are presented by filled symbols. The results show good agreement with experiment with a slight under-prediction of IDT as expected (0.34 and 0.39 ms in simulation and experiments, respectively). This earlier ignition is attributed to the simplified low-temperature oxidation kinetics of the Yao et al. mechanism [81]. It is seen that the IDT increases with ϕ_{CH_4} . The observation on IDT is consistent with the experiments [18–20] and the results for zero- and one-dimensional simulation. Both the first- and second-stage ignition are delayed by an increased ϕ_{CH_4} . However, the duration of the cool flame period, 0.213 ms, 0.218 ms, and 0.220 ms for the DF1, DF2, and DF3 cases, respectively, remains nearly constant, indicating the majority of the retarding effect acts on the first-stage ignition. The increments of LTC account for 85.8, 83.9, and 76.4% of the increased IDT for DF1, DF2, and DF3, respectively. This is in accordance with the observation for DF ignition that the delay of LTC represents 70 to 80% of total increased IDT [21]. The period between τ_{HTC} and IDT slightly increases as ϕ_{CH_4} increases, illustrating a retarding effect of ambient methane on the formation of OH. A clear dependency of LOL to ϕ_{CH_4} is predicted. Further analysis of ignition behavior will be discussed in detail in the following sections.

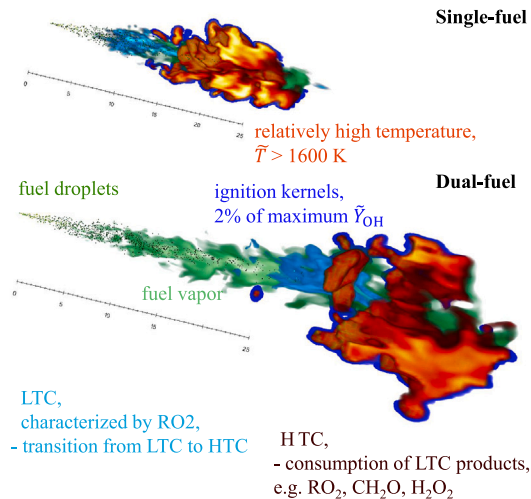


Fig. 9. Volume rendered illustration of the comparison between a typical spray ignition (upper) and a dual-fuel pilot spray ignition (DF2, lower) at the instance of IDT. The colors correspond to fuel vapor $Z > Z_{MR,HTC}$ (gray), RO_2 (sky blue), ignition kernels (admiral blue), and $\bar{T} > 1600$ K (yellow). Fuel droplets are indicated by green dots. (For interpretation of the references to color in this figure legend, the reader is referred to the web version of this article.)

4.3.3. Spatial and temporal evolution of spray flame structure

This section focuses on the ignition characteristics of different DF sprays in comparison to the baseline SF case. A straightforward impression of SF and DF combustion can be seen via the flame structure at IDT in Fig. 9. A transition from liquid fuel evaporation to turbulent fuel–air mixing, LTC, and HTC is observed in both cases. In the following, LTC and HTC for all cases are quantitatively identified and analyzed with respect to flame development.

Figs. 10 and 11 include the transient stages of the ignition process for SF (left-hand-side of the odd-line) and DF (others) cases. The combustion processes for all cases are sampled according to the two-stage ignition characteristics, including time instances correspond to: (I) approximately at the first-stage ignition (τ_{LTC}) when LTC is initiated, (II) at the onset of the second-stage ignition (τ_{HTC}) when HTC is observed together with LTC, (III) the IDT, (IV) at 1.5IDT as a representative of the quasi-steady flame and (V) uniformly at 2 ms to discard the significant differences in spray development corresponding to stage I–IV.

Fig. 10 shows the temperature field evolution in time. The corresponding mixture fraction distribution is depicted in Fig. 11 to explore the role of turbulent mixing on ignition characteristics. In both figures, a dotted line is used to indicate the stoichiometric mixture fraction Z_{st} . To locate the boundary of the spray envelope, the mixture fraction field is embedded with green dashed line corresponding to an equivalence ratio ϕ of 0.01. Although the mixture distribution significantly varies

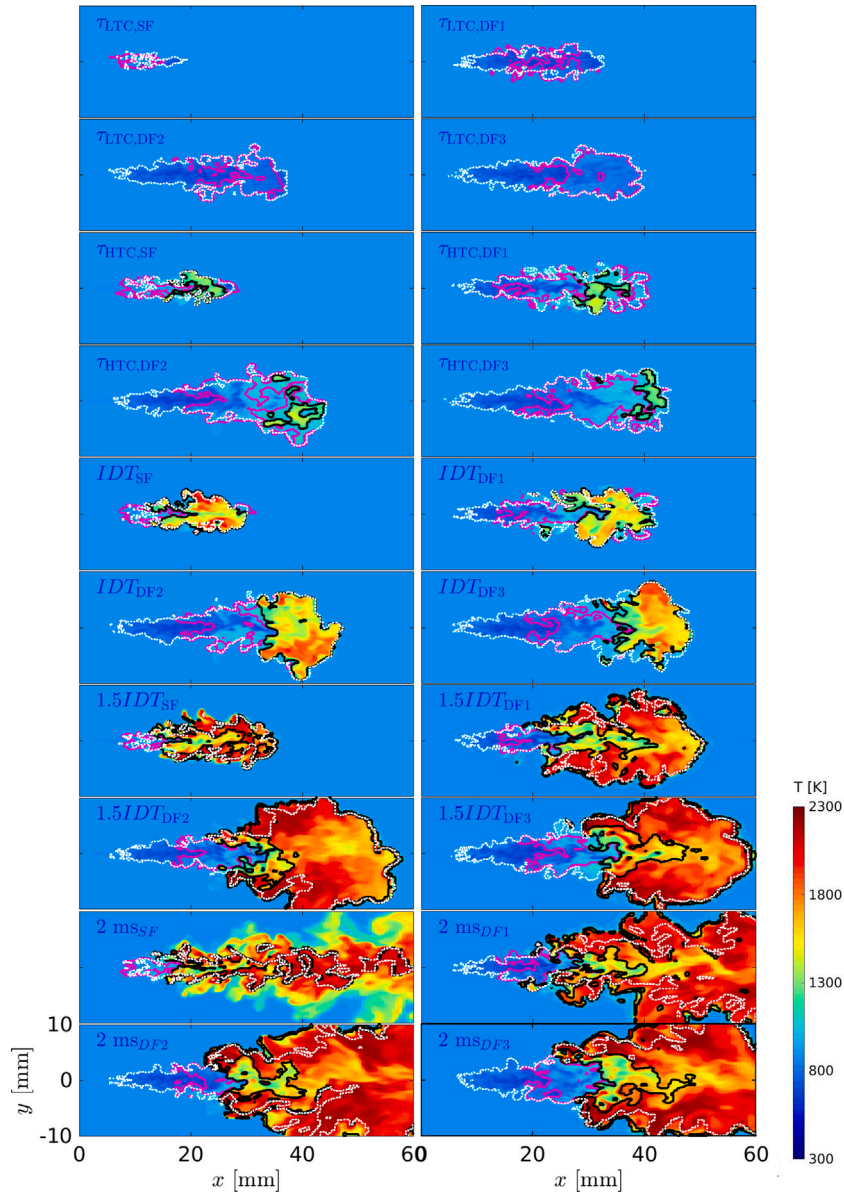


Fig. 10. Temporal temperature evolution for characteristic time instances. For each time instance, the four cases (SF, DF1, DF2, and DF3) are arranged from left to right and from top to bottom. The LTC and HTC region are marked by magenta solid line (—) and black solid line (—), respectively. White dotted line represents the stoichiometric mixture fraction. (For interpretation of the references to color in this figure legend, the reader is referred to the web version of this article.)

between cases, it is seen that the Z_{st} contour for each case appears at the same axial distance to the injector exit at all selected time instances. In reacting SF spray, this distance was found to be closely related to the inception of LTC both experimentally [82] and numerically [44]. However, this is not the case for DF cases as ϕ_{CH_4} increases. It is clearly seen in Fig. 10 that for higher ϕ_{CH_4} , LTC tends to initialize farther downstream of the Z_{st} onset. In Fig. 9, it is observed that the LTC region partially envelopes the fuel droplets for the SF flame, while in the $\phi_{CH_4} = 0.5$ case the LTC region is downstream of the region with liquid penetration. Next, the two figures are analyzed together to address the effect of ϕ_{CH_4} on ignition behavior. We subsequently focus on τ_{LTC} , τ_{HTC} and IDT.

At τ_{LTC} (the first and second rows of Figs. 10 and 11), the reaction is dominated by LTC marked by a magenta solid line (—). The boundary of the LTC region is defined as the isoline of 1% of maximum \tilde{Y}_{RO_2} ever in the domain ($\tilde{Y}_{RO_2} > 0.01 * \tilde{Y}_{RO_2}^{max}$). It is noted that τ_{LTC} value increases with ϕ_{CH_4} , such that the spray region varies. Recently, spray ignition has been found to be highly correlated with the ignition of vapor fuel in the spray that is close to the most reactive mixture [83,84].

According to the results shown in Fig. 1, leaner mixtures for all the simulated cases are more reactive regarding LTC ($Z < 0.05$). Indeed, in all cases, the LTC occurs in a relatively lower mixture fraction region. In turbulence, a higher τ_{LTC} corresponds to a longer duration of fuel–air mixing and subsequently a more diluted gaseous fuel near the spray tip, enabling spatially wider distributed combustion. The LES results show that an increased ϕ_{CH_4} leads to a broader LTC region as a result of the prolonged τ_{LTC} . Although both the SF and DF cases are more reactive in similar lean mixtures, the initialization of LTC shifts to farther downstream from the injector tip as ϕ_{CH_4} increases. This is attributed to the higher strain rate near the nozzle outlet. As is seen in Fig. 3, the retarding effect of strain rate on τ_{LTC} is more prominent as ϕ_{CH_4} increases. Hence, the higher strain rate in the upstream of spray hampers the initialization of LTC more and more as ϕ_{CH_4} increases.

At τ_{HTC} (the third and fourth rows of Figs. 10 and 11), the initialization of HTC is observed, which is indicated by black (—) and yellow (—) solid line in Figs. 10 and 11, respectively. As is already discussed, the identification of HTC region follows H_2O_2 decomposition rather than a temperature threshold. Here, HTC is considered to be

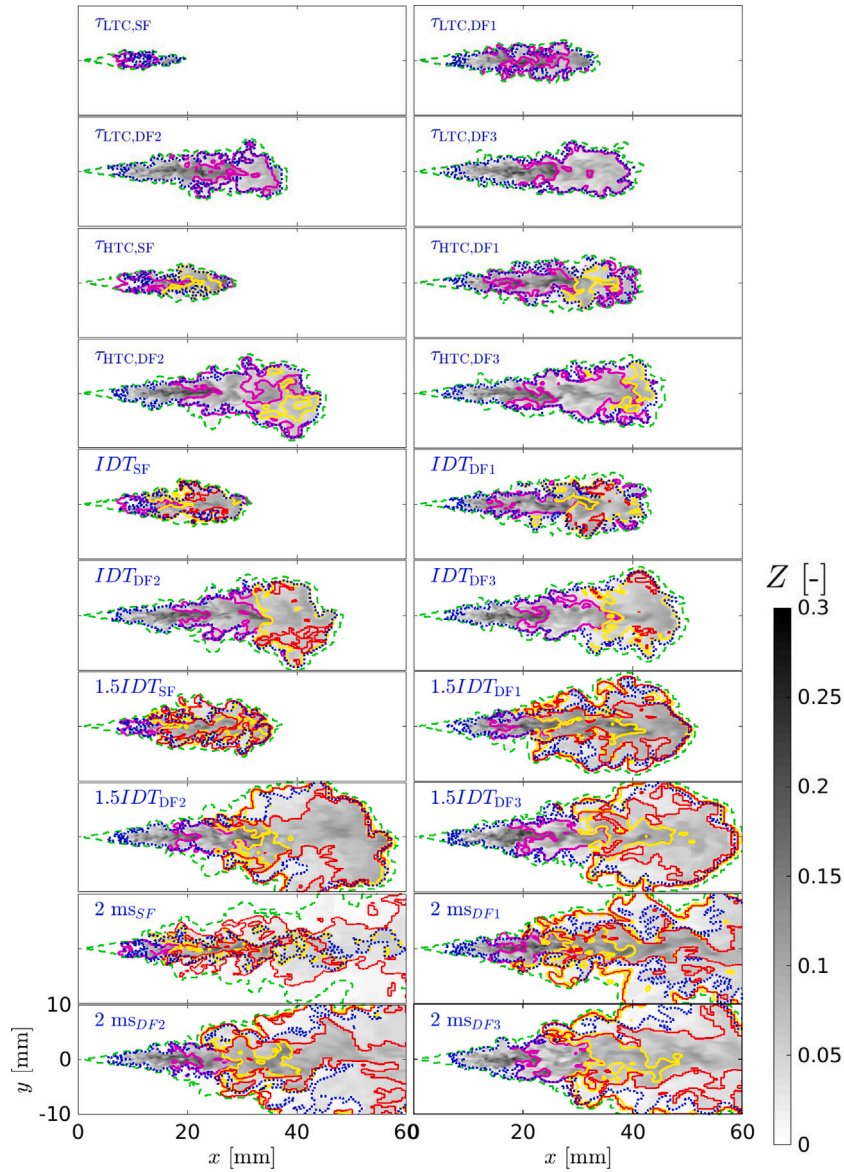


Fig. 11. Spatial distribution of mixture fraction within the spray envelope ($\phi > 0.01$, colored by green dashed line $-\cdot-\cdot-$). The order of sub-figures are arranged as in Fig. 10. The LTC and HTC region are marked by magenta solid line ($---$) and yellow solid line ($---$), respectively. Red solid line corresponds to ignition kernels ($\tilde{Y}_{OH} > 2\% \tilde{Y}_{OH}^{max}$, $---$). Blue dotted line ($.....$) represents the stoichiometric mixture fraction. (For interpretation of the references to color in this figure legend, the reader is referred to the web version of this article.)

activated when the local consumption rate of H_2O_2 is greater than 1% of the maximum value found in the domain during its evolution ($\tilde{\omega}_{H_2O_2} > 0.01 * \tilde{\omega}_{H_2O_2}^{max}$ & $\tilde{T} > 1150$ K). Additionally, also a temperature threshold of 1150 K is adopted following literature [73]. Compared to the contour plots at τ_{LTC} , a growth of LTC region is seen. In each case, the LTC rendering envelope develops towards the spray tip from τ_{LTC} . The HTC is directly a consequence of the LTC products accumulation, and thus initializes within the LTC region. Onset of the HTC is at a somewhat higher distance from nozzle outlet as ϕ_{CH_4} increases. For all cases, heat release (region with temperature rise, i.e. colored by bright blue and green) occurs mainly at the spray head and is attributed to both LTC and HTC according to Fig. 10. An interesting observation is that the LTC region seems to be “broken” by the HTC envelope (the HTC contour appears within the LTC contour) at lower ϕ_{CH_4} . This will be further analyzed later in this section.

The fifth and sixth rows of Figs. 10 and 11 illustrate the ignition characteristics at IDT. This time instance characterizes the onset of local high-temperature oxidation among reaction products towards the equilibrium. It is always followed by a rapid increase in temperature

(high gradient of temporal maximum temperature evolution in the domain) [40]. In Fig. 11, the corresponding region is visualized by red solid line ($---$), representing the formation of high temperature ignition kernels where local \tilde{Y}_{OH} is greater than 2% of its maximum value in the domain during simulation ($\tilde{Y}_{OH} > 0.02 * \tilde{Y}_{OH}^{max}$). The ignition kernels at multiple sites are found to first appear at the periphery of the spray aligned to the contour of Z_{st} . Similar to the observation on HTC, its onset distance to the nozzle outlet increases with ϕ_{CH_4} . The HTC for all cases at IDT is observed to cover the whole spray head. It propagates not only to the downstream but also to the upstream part of the spray that is close to the injector tip. The difference in highest temperature among cases at this characteristic time instance justifies the observation in Ref. [24,57] that the IDT in a DF configuration cannot be identified by a temperature threshold.

4.3.4. Flame development after the IDT

Both the forth and fifth time instances in Figs. 10 and 11 correspond to the “quasi-steady” state flame, corresponding to 1.5IDT and 2 ms,

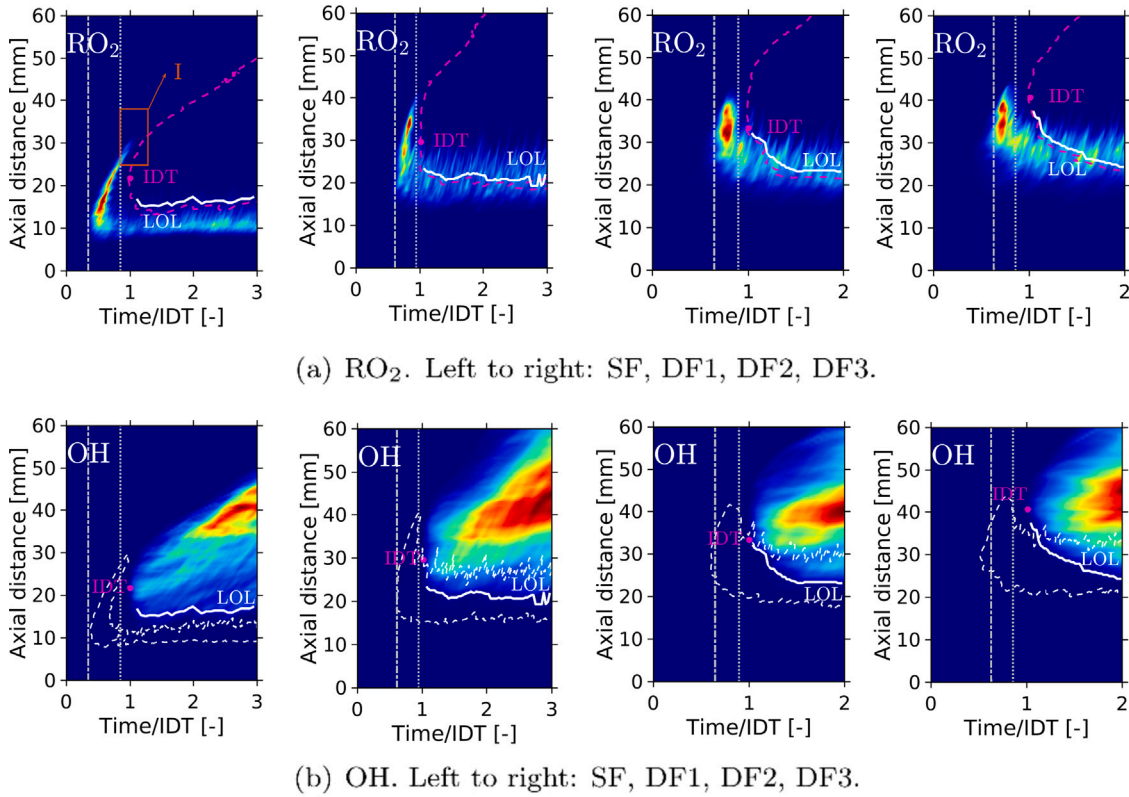


Fig. 12. I_{xt} -plots of RO_2 and OH for a variety of ϕ_{CH_4} . Red color represents maximum intensity, while blue color refers to minimum intensity (the intensity of a species refers to the percentage of its maximum mass fraction). τ_{LTC} and τ_{HTC} are marked by a vertical gray dashed-dotted line (-----) and a vertical gray dotted line (.....), respectively. The LOL is depicted by a white curve. The magenta point indicates the IDT. For convenience, the boundary of the OH contour (1% of $I_{xt,\text{OH}}|_{\text{max}}$) is highlighted with a magenta dashed line (---) in I_{xt,RO_2} , while the boundary of the RO_2 contour (1% of $I_{xt,\text{RO}_2}|_{\text{max}}$) is labeled by a white dashed line in $I_{xt,\text{OH}}$. (For interpretation of the references to color in this figure legend, the reader is referred to the web version of this article.)

respectively. Common characterizations in this stage can be summarized for the four cases. From the instance defined by IDT, the HTC develops not only downstream following the development of spray tip but also towards the nozzle, and finally settles at the LOL. The onset of LTC, on the other hand, remains at the same axial distance to the injector in this period. Meanwhile, the tip of LTC shifts back to the upstream region until an equilibrium is achieved. The ignition kernels keep expanding around the Z_{st} contour tending to merge at the spray tip first and subsequently propagate to the downstream of the spray. The existence of methane in the background does not alter the trend observed for standard Spray A (SF case) in literature [23,85]. An interesting observation is that the vicinity of the spray envelope for the SF case experiences a moderate temperature at 2 ms compared to that at 1.5IDT. At 2 ms, although HTC is still confined within the Z_{st} contour, the ignition kernels are spatially more widely distributed. This is strongly associated to the separation between the Z_{st} contour and the spray boundary, which does not happen in non-reacting sprays. The shrinking of the domain enclosed by the Z_{st} contour is attributed to the result of high-temperature oxidation, as the mixture fraction values are observed to develop towards lower than Z_{st} only in the HTC region but not in the LTC zone. This separation is also seen in DF cases. However, 2 ms seems not long enough for the DF cases to form green-lighted reaction region in the vicinity of flame as seen in the SF case. Nevertheless, the separation of Z_{st} contour and the spray boundary at 2 ms is more prominent for lower ϕ_{CH_4} . This corroborates the observation that the effect of methane on LTC is lower for lower ϕ_{CH_4} .

Further information on ignition behavior for different ϕ_{CH_4} can be obtained from the I_{xt} -plots. Fig. 12 contains I_{xt} -plots of OH and RO_2 as markers for HTC and LTC, respectively. In both cases, red correlates with maximum intensity and blue refers to minimum intensity. Here,

the intensity of a species has been normalized using the maximum mass fraction value during simulation. For convenience, time is scaled by their IDT. For all cases, the two-stage combustion feature is confirmed due to the fact that RO_2 appears earlier than the IDT while OH is only found after approximately the IDT. The intensity of RO_2 has a maximal value after τ_{LTC} , followed by its consumption before OH production takes place and a relatively stabilized low-level RO_2 intensity is achieved. The trend is similar to the development of formaldehyde in the pre-mixed burn phase observed in experiments [82,86]. The region of high-intensity RO_2 is found between τ_{LTC} and τ_{HTC} , i.e. the cool flame period, illustrating RO_2 to be a representative species correlating with the LTC. Spatially, RO_2 expands not only towards the downstream part but also to the upstream part of the spray region. This cool flame wave was also observed by Dahms et al. within Spray A [87].

As ϕ_{CH_4} increases, the cool flame seems to shift a longer distance upstream from its initialization location. It is noted that in the SF case, the high-intensity of RO_2 appears simultaneously in both the upstream (see region I in Fig. 12(a)) and downstream region after the cool flame period, i.e. after τ_{HTC} , while no high-intensity is seen in the middle-region. This supports the observation in Figs. 10 and 11 that the LTC region is interrupted by the HTC at lower ϕ_{CH_4} . For higher ϕ_{CH_4} , the spatially separated cool flame wave is not seen.

$I_{xt,\text{OH}}$ peaks in the upper right corner of the luminous contour, corresponding to a location farther downstream from the injector. The high-intensity distribution of OH hardly overlaps with that of RO_2 . This is attributed to the fact that they are respective products of different combustion phase. However, the low-intensity part of RO_2 and OH overlap around the LOL. The I_{xt} -plots illustrate that the two species, RO_2 and OH, appear at the same axial distance to the injection tip. This does not mean they co-exist at the same location as the I_{xt} distribution is radially integral. The spatial co-existence will be investigated and

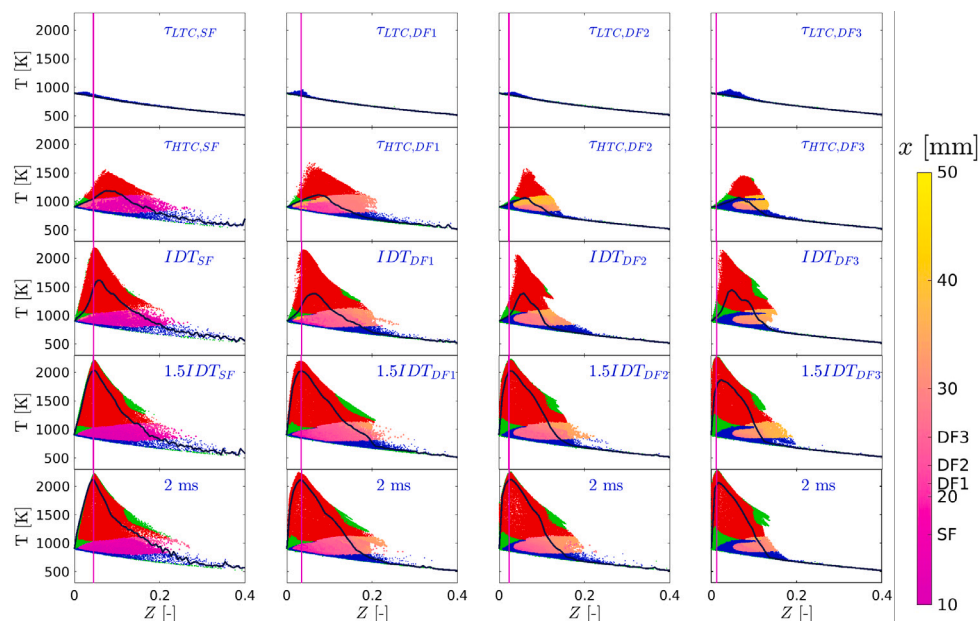


Fig. 13. Temperature evolution in mixture fraction space within the spray envelope. The LTC region is marked by blue color, while the HTC region is denoted by red color. The location where both LTC and HTC occur is colored by its axial distance from the injector tip using the color scheme indicated on the RHS of the figure. The LOL for the four simulated cases is indicated on the color legend. Green color indicates neither LTC nor HTC. Z_{st} is marked by vertical solid line. The black solid line represents the mean temperature conditioned with respect to mixture fraction. (For interpretation of the references to color in this figure legend, the reader is referred to the web version of this article.)

discussed in the following section. Although for all cases the OH keeps accumulating until the last time instance plotted, its onset remains at the same axial distance from the injector. The LOL indicated on the bottom of OH luminous region initializes in the downstream of spray with a change in time shortly after IDT, and finally is tending to level-off at a decreased axial distance from the nozzle. The speed at which this settling happens decreases with ϕ_{CH_4} . For $\phi_{CH_4} = 0.75$, the LOL is still not yet stabilized for the time shown. This illustrates the retarding effect of ambient methane on the HTC.

4.3.5. Flame development in mixture fraction space

This section investigates the influence of ϕ_{CH_4} on the combustion characteristics in mixture fraction space. In Fig. 13, the spatial flame development depicted in Fig. 10 is mapped to temporal evolution with respect to filtered mixture fraction. For visibility, only the information within the spray envelope ($\phi > 0.01$) is addressed. The scatter points are categorized according to stages of combustion. LTC and HTC are represented by blue and red points, respectively. The green colored data belong to neither LTC nor HTC. To identify the interaction between LTC and HTC, situations for which both LTC and HTC occur are colored by their axial distance to the nozzle outlet. The conditional mean temperature with respect to mixture fraction is introduced by black solid line. It is obtained from the filterer fields computed by LES without considering the subgrid effects.

The two-stage combustion feature of both SF and DF cases are confirmed by the scatter plots considering the fact that only LTC is seen among the scatter points in the first row (at τ_{LTC}). The temperature within the spray region for DF cases, peaks at similar values of mixture fraction, whereas the peak of SF case correlates with a slightly lower value of Z . This is consistent with the observation in zero-dimensional simulation. No significant difference in $Z_{MR,LTC}$ exists for DF cases while the $Z_{MR,LTC}$ for SF is slightly lower.

At τ_{HTC} , a higher ϕ_{CH_4} leads to a narrower distribution of scatter points in the mixture fraction space. According to the conditional averaged temperature profiles, the richest mixture where a temperature rise (deviation from the inert mixing) is seen shifts to a leaner value, i.e. spatially corresponding to more diluted fuel, for higher ϕ_{CH_4} . This is

attributed to the higher dilution due to the increased available mixing time induced by the increasing τ_{LTC} as function of ϕ_{CH_4} , as was pointed out by Kahila et al. [57]. Besides, for higher ϕ_{CH_4} , lower conditional averaged temperature values are seen at rich mixture conditions (e.g. $Z > 0.1$). This illustrates that apart from the constraints of dilution, the addition of methane retards the reactions in rich mixtures as well. On the contrary, the peak temperature at τ_{HTC} for lower ϕ_{CH_4} appears in leaner mixtures. This is consistent with the observation in zero-dimensional simulation where it was found that $Z_{MR,HTC}$ increases with ϕ_{CH_4} .

After τ_{HTC} , the distribution of scatter points in $Z - T$ plane experience rapid change until the IDT for all cases, followed by stabilization afterwards. However, although no significant change in $Z - T$ plots is seen after IDT, the peaks of conditional averaged temperature profile gradually rise. This illustrates continuous flame development towards HTC, which is visualized in both the temperature fields Fig. 10 and $I_{x,OH}$ -plots Fig. 12(b). In general, combustion of both SF case and DF cases develop to richer mixtures at first and shift back towards a stabilization at Z_{st} . This is in line with the observation for SF ignition [23,85,87].

The $Z - T$ plots confirm that LTC and HTC may occur simultaneously. For a certain ϕ_{CH_4} , the distribution of these overlapped scatter points, denoted by LHCTC for brevity, remains unchanged with respects to Z after τ_{HTC} . It is noted that for lower ϕ_{CH_4} , the distribution of LHCTC covers a wider range of Z values. As indicated by the color, in all simulated cases, the LHCTC spatially cover regions farther downstream of the spray in the beginning, and stabilize at the upstream side as combustion proceeds. The spatial evolution of LHCTC seems to align with that of LOL shown in Fig. 12. This is due to the fact that HTC is a result of accumulation of LTC products, and that the flame stabilizes where transition from LTC to HTC occurs.

4.3.6. Analysis of combustion mode

In this section, the CEMA-based criterion is utilized to unravel the structure of the four investigated flames. The spatial combustion mode distributions are shown in Fig. 14 for selected phases of ignition. As a comparison, in Fig. 15, the corresponding combustion mode segmentation are revealed in $Z - T$ space.

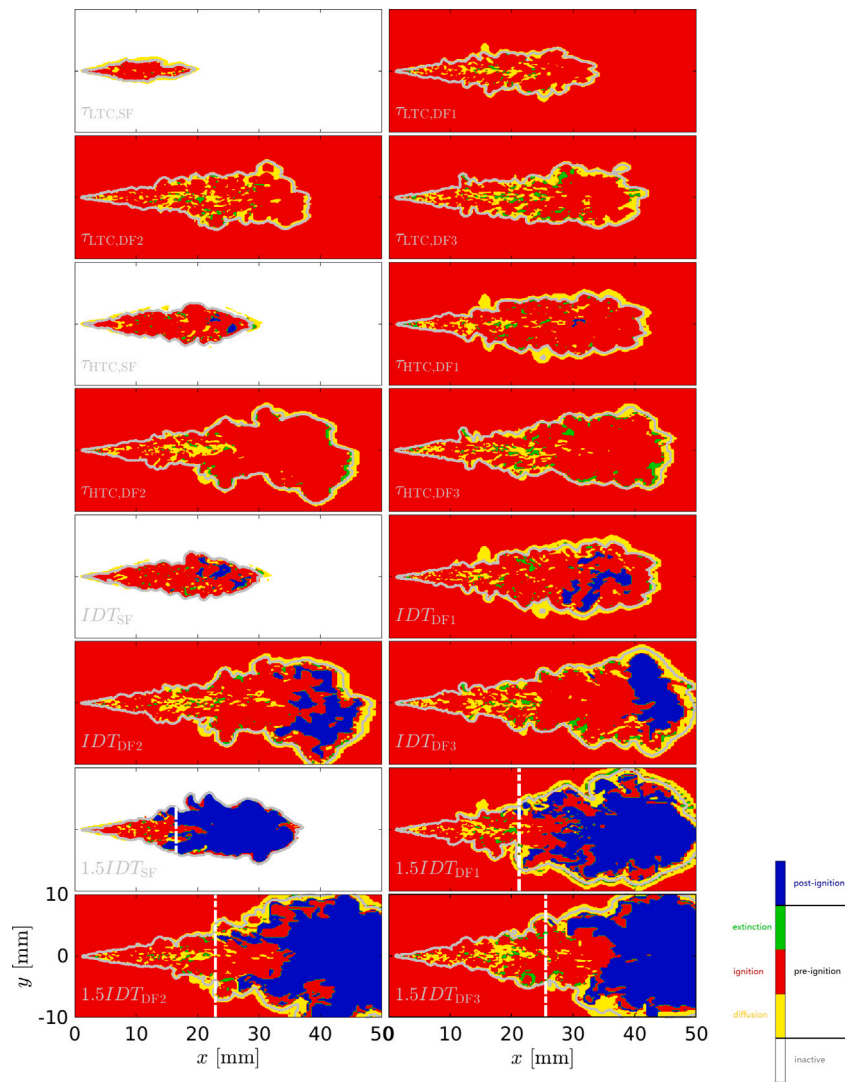


Fig. 14. Combustion mode segmentation in a selected plane across the spray axis. The post-ignition and inactive modes are marked by blue and white color, respectively. The pre-ignition mode is characterized by different colors (yellow: diffusion, red: ignition, green: extinction). The gray solid lines (—) correspond to the spray boundary ($\phi=0.01$), with the LOL marked by white dashed lines. (For interpretation of the references to color in this figure legend, the reader is referred to the web version of this article.)

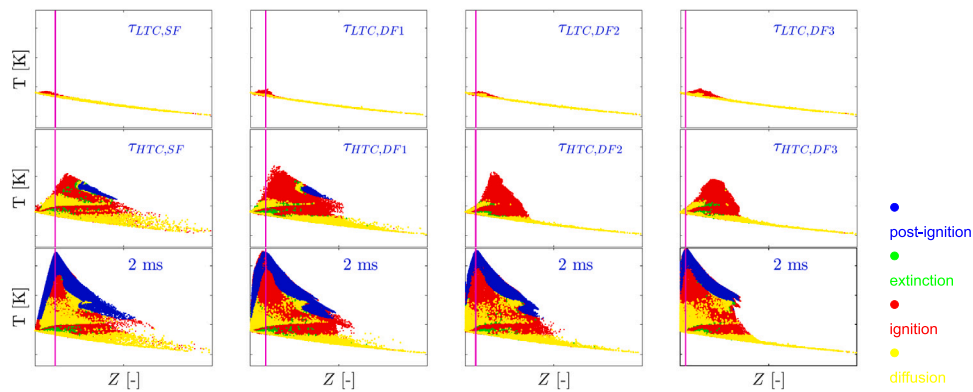


Fig. 15. Temperature distribution in mixture fraction space at representative time instances, colored by chemical explosive modes (•: post-ignition, •: extinction, •: ignition, •: diffusion). Vertical lines are Z_{st} . (For interpretation of the references to color in this figure legend, the reader is referred to the web version of this article.)

At τ_{HTC} , the diagnosed combustion mode distribution for SF and DF cases are similar within the flame envelope. Spatially, the vicinity of the flame envelope is dominated by the diffusion mode, while the

ignition mode is much more dominant at the flame tip. Both modes are widely distributed in mixture fraction space. In rich mixtures, the diffusion mode is more frequently present than the ignition mode. This

is due to the fact that heat release rising from auto-ignition in the most reactive mixtures (Z_{MR}) propagates to the surrounding. Until τ_{HTC} , all local flame structures are pre-ignition mixtures as expected. At τ_{HTC} , a significant difference in combustion mode is seen among different cases. For lower ϕ_{CH_4} , post-ignition mixtures initialize while for higher ϕ_{CH_4} the sprays are still composed of pre-ignition mixtures. As post-ignition mixture is directly a consequence of HTC, CEMA analysis confirms the postponed HTC under the presence of ambient methane. Although the post-ignition mode only occupies a limited region within the flame envelope, a relatively wider distribution in mixture fraction space is observed. After IDT, the post-ignition region expands to more regions within the downstream of region of the flame, aligning with the high temperature region seen in Fig. 10. It is seen that in the vicinity of the flame envelope in the downstream region for the DF case the combustion mode is dominated by diffusion, while on the contrary for the SF case it is fully composed of ignition and post-ignition mixtures, i.e. the HTC. In mixture fraction space, post-ignition mode extends toward both richer and leaner mixtures. The development of post-ignition flame towards the downstream region, i.e. leaner mixtures, is bounded by the penetration of fuel vapor. On the other hand, the propagation of the post-ignition mode to the richer side is restricted as ϕ_{CH_4} increases. This is attributed to the effect of ambient methane on ignition in the rich mixtures.

In general, as ϕ_{CH_4} is increased, the diffusion mode is more prominent in rich mixtures near the adiabatic mixing line, spatially corresponding to the most upstream part of the spray. This can be seen via the spatial distribution of combustion mode depicted in Fig. 14. The LHTC zone, shown in Fig. 13, that is close to the LOL is observed to be dominated by the ignition mode according to Fig. 15. A close correlation is seen for the boundary of diffusion and the ignition flame mode within this region at relatively low temperature. This illustrates that the transition from LTC to HTC is not only due to ignition, but also a result of diffusion. However, the diffusion mode is restricted to leaner mixtures. This is in accordance with the observation by Zhang et al. on mixtures at the LOL [88]. For higher ϕ_{CH_4} , post-ignition mixtures exist further downstream of the LOL as is depicted in Fig. 14. Also, post-ignition mixtures for increased ϕ_{CH_4} correspond to higher temperature according to Fig. 15. For the SF case, HTC products are predicted to extend to the upstream of the LOL and rich mixtures, as was experimentally observed by Sim et al. [82].

5. Conclusions

The present work studies the effect of ambient methane on ignition behavior of an *n*-dodecane turbulent spray using numerical modeling. A key component of the modeling is the FGM approach based on a range of flamelets with different strain rate. The quality of the FGM tabulation is first verified by applying it to laminar counterflow flames and then applied in combination with LES.

The igniting spray simulations are based on the extensively numerically validated ECN Spray A case. *n*-dodecane as pilot spray is injection into a constant-volume filled with lean methane–air mixture at engine-like condition. By adding methane to ambient oxidizer of the baseline Spray A condition, different lean fuel–air mixtures are achieved. Subsequently, ignition behavior of selected conditions are studied and compared in zero-, one-, and three-dimensional simulations. The resulting combustion behavior is analyzed in detail with respect to ambient methane–air equivalence ratio. In both the SF and DF cases, ignition can be characterized by a LTC phase and a HTC phase. According to the simulated results, both LTC and HTC are influenced by ambient methane. The initialization of both LTC and HTC are observed to be consistently retarded with increased ϕ_{CH_4} , while the induction time between LTC and HTC are relatively less sensitive to ϕ_{CH_4} compared to the IDT. The observation supports the observation in experiments [18–20], suggesting that the simulation approach is reliable. It is found that LTC and HTC are more prolonged in higher dimensional simulation

as a consequence of mixing. Further information is summarized in the following.

For an igniting spray, LTC predominantly starts in diluted mixtures close to the $Z_{MR,LTC}$ given by zero-dimensional simulation. Spatially, LTC initializes farther downstream from the injector tip as ϕ_{CH_4} increases. Within a flamelet framework, an enhanced retarding effect of strain rate on LTC is found for higher ϕ_{CH_4} . High strain rate in the upstream hampers the initialization of LTC, especially for higher ϕ_{CH_4} cases. A higher ϕ_{CH_4} leads to volumetric broader LTC distribution due to more diluted fuel at the spray tip as a consequence of prolonged mixing. LTC propagates to the downstream region with a velocity that is higher than that of the spray tip. Initialization of HTC is more probable to occur in rich mixtures. As a consequence of LTC products, HTC accumulation initializes within the LTC region. The transition from LTC to HTC spatially evolves in time and aligns with the evolution of the LOL.

CEMA analysis illustrates that an increased ϕ_{CH_4} correlates with more prominent inhibition of ignition in rich mixtures. The outer region of the flame for the DF cases is persistently more dominated by diffusion rather than ignition. The transition from LTC to HTC, i.e. flame stabilization, is mainly driven by both ignition and diffusion (assisted auto-ignition), while the diffusion mode mainly acts on leaner mixtures.

All together, the different methods of analysis used in this work provide detailed understanding of ignition and evolution of spray flame development and are applicable for a wide range of fuels and operating conditions.

CRedit authorship contribution statement

Hesheng Bao: Writing – review & editing, Writing – original draft, Software, Methodology, Formal analysis, Data curation, Conceptualization. **Jinlin Han:** Writing – review & editing, Conceptualization. **Yan Zhang:** Software. **Andrea Di Matteo:** Data curation. **Dirk Roekaerts:** Writing – review & editing, Supervision. **Jeroen Van Oijen:** Writing – review & editing. **Bart Somers:** Writing – review & editing, Supervision.

Declaration of competing interest

The authors declare that they have no known competing financial interests or personal relationships that could have appeared to influence the work reported in this paper.

Data availability

Data will be made available on request.

Acknowledgment

The authors are grateful to Tianfeng Lu and Ji-Woong Park from University of Connecticut for help with applying the chemical explosive mode analysis.

Appendix. The optimized progress variable

See Table A.2.

Table A.2

Optimized coefficients adopted for the progress variable.

N2	0	nC3H7	4947.7853
AR	0	C2H3CHO	66139.6211
H	-249135.8386	C4H7	74398.233
O	286100.6433	C4H81	-18103.3017
OH	-88734.2915	pC4H9	87201.3344
HO2	-160481.1797	C5H9	-106944.409
H2	-162775.1588	C5H10	37160.9634
H2O	784647.1556	PXC5H11	-79093.7313
H2O2	-175530.1866	C6H12	-316988.545
O2	-621028.661	PXC6H13	-51244.7358
CH2	-61220.1101	C7H14	-177036.3807
CH2*	269911.2396	PXC7H15	47159.7817
CH3	-150702.9488	C8H16	-232714.3679
CH4	-382348.0388	PXC8H17	41919.1676
HCO	-60372.395	C9H18	58935.8203
CH2O	-296258.5625	PXC9H19	-202180.8399
CH3O	-224038.8396	C10H20	393013.3111
CO	-526693.1596	PXC10H21	177447.7354
CO2	-140518.9854	NC12H26	-235742.4876
C2H2	97452.0616	PXC12H25	-118523.3703
C2H3	187683.3535	SXC12H25	175773.9776
C2H4	-81055.799	S3XC12H25	-5817.1062
C2H5	-155247.6628	C12H24	-57295.8846
C2H6	-75474.9285	C12H25O2	92606.2167
CH2CHO	-102855.8354	C12OOH	29513.6773
aC3H5	-153014.8464	O2C12H24OOH	-354862.7187
C3H6	-26453.4317	OC12H23OOH	465979.467

References

- [1] Saxena S, Bedoya ID. Fundamental phenomena affecting low temperature combustion and HCCI engines, high load limits and strategies for extending these limits. *Prog Energy Combust Sci* 2013;39(5):457–88.
- [2] Han J, Bao H, Somers L. Experimental investigation of reactivity controlled compression ignition with n-butanol/n-heptane in a heavy-duty diesel engine. *Appl Energy* 2021;282:116164.
- [3] Han J, Somers B. Effects of butanol isomers on the combustion and emission characteristics of a heavy-duty engine in RCCI mode. *SAE Technical Paper*, 2020, p. 0307.
- [4] Reitz RD. Directions in internal combustion engine research. *Combust Flame* 2013;160(1):1–8.
- [5] Han J, He W, Somers L. Experimental investigation of performance and emissions of ethanol and n-butanol fuel blends in a heavy-duty diesel engine. *Front Mech Eng* 2020;6:26.
- [6] Han J, Somers L, Cracknell R, Joedicke A, Wardle R, Mohan VRR. Experimental investigation of ethanol/diesel dual-fuel combustion in a heavy-duty diesel engine. *Fuel* 2020;275:117867.
- [7] Wei L, Geng P. A review on natural gas/diesel dual fuel combustion, emissions and performance. *Fuel Process Technol* 2016;142:264–78.
- [8] Sahoo B, Sahoo N, Saha U. Effect of engine parameters and type of gaseous fuel on the performance of dual-fuel gas diesel engines—A critical review. *Renew Sustain Energy Rev* 2009;13(6–7):1151–84.
- [9] Dronniou N, Kashdan J, Lecoite B, Sauve K, Soleri D. Optical investigation of dual-fuel CNG/Diesel combustion strategies to reduce CO₂ emissions. *SAE Int J Engines* 2014;7(2):873–87.
- [10] Nithyanandan K, Gao Y, Wu H, Lee C-F, Liu F, Yan J. An optical investigation of multiple diesel injections in CNG/diesel dual-fuel combustion in a light duty optical diesel engine. *SAE Technical Paper*, 2017, p. 0755.
- [11] Khosravi M, Rochussen J, Yeo J, Kirchen P, McTaggart-Cowan G, Wu N. Effect of fuelling control parameters on combustion characteristics of diesel-ignited natural gas dual-fuel combustion in an optical engine. In: *ASME 2016 internal combustion engine division fall technical conference*, vol. 50503. American Society of Mechanical Engineers Digital Collection; 2016, V001T03A012.
- [12] Ahmad Z, Aryal J, Ranta O, Kaario O, Vuorinen V, Larmi M. An optical characterization of dual-fuel combustion in a heavy-duty diesel engine. *SAE Technical Paper*, 2018, p. 0252.
- [13] Ma X, Qi Y, Wang Z, Xu H, Wang J-X. An experimental study of EGR-controlled stoichiometric dual-fuel compression ignition (SDCI) combustion. *SAE Technical Paper*, 2014, p. 1307.
- [14] Aksu C, Kawahara N, Tsuboi K, Kondo M, Tomita E. Extension of PREMIER combustion operation range using split micro pilot fuel injection in a dual fuel natural gas compression ignition engine: A performance-based and visual investigation. *Fuel* 2016;185:243–53.
- [15] Grochowina M, Schiffner M, Tartsch S, Sattelmayer T. Influence of injection parameters and operating conditions on ignition and combustion in dual-fuel engines. *J Eng Gas Turbines and Power* 2018;140(10):102809.
- [16] Schlatter S, Schneider B, Wright Y, Boulouchos K. Experimental study of ignition and combustion characteristics of a diesel pilot spray in a lean premixed methane/air charge using a rapid compression expansion machine. *SAE Technical Paper*, 2012, p. 0825.
- [17] Schlatter S, Schneider B, Wright YM, Boulouchos K. Comparative study of ignition systems for lean burn gas engines in an optically accessible rapid compression expansion machine. *SAE Technical Paper*, 2013, p. 0112.
- [18] Schlatter S, Schneider B, Wright YM, Boulouchos K. N-heptane micro pilot assisted methane combustion in a Rapid Compression Expansion Machine. *Fuel* 2016;179:339–52.
- [19] Srna A, von Rotz B, Herrmann K, Boulouchos K, Bruneaux G. Experimental investigation of pilot-fuel combustion in dual-fuel engines, part 1: Thermodynamic analysis of combustion phenomena. *Fuel* 2019;255:115642.
- [20] Srna A, von Rotz B, Bolla M, Wright YM, Herrmann K, Boulouchos K, Bruneaux G. Experimental investigation of pilot-fuel combustion in dual-fuel engines, part 2: Understanding the underlying mechanisms by means of optical diagnostics. *Fuel* 2019;255:115766.
- [21] Srna A, Bolla M, Wright YM, Herrmann K, Bombach R, Pandurangi SS, Boulouchos K, Bruneaux G. Effect of methane on pilot-fuel auto-ignition in dual-fuel engines. *Proc Combust Inst* 2019;37(4):4741–9.
- [22] Skeen SA, Manin J, Pickett LM. Simultaneous formaldehyde PLIF and high-speed schlieren imaging for ignition visualization in high-pressure spray flames. *Proc Combust Inst* 2015;35(3):3167–74.
- [23] Kahila H, Wehrfritz A, Kaario O, Masouleh MG, Maes N, Somers B, Vuorinen V. Large-eddy simulation on the influence of injection pressure in reacting Spray A. *Combust Flame* 2018;191:142–59.
- [24] Kahila H, Kaario O, Ahmad Z, Masouleh MG, Tekgül B, Larmi M, Vuorinen V. A large-eddy simulation study on the influence of diesel pilot spray quantity on methane-air flame initiation. *Combust Flame* 2019;206:506–21.
- [25] Wei H, Zhao W, Qi J, Liu Z, Zhou L. Effect of injection timing on the ignition process of n-heptane spray flame in a methane/air environment. *Fuel* 2019;245:345–59.
- [26] Tekgül B, Kahila H, Kaario O, Vuorinen V. Large-eddy simulation of dual-fuel spray ignition at different ambient temperatures. *Combust Flame* 2020;215:51–65.
- [27] Bhagatwala A, Sankaran R, Kokjohn S, Chen JH. Numerical investigation of spontaneous flame propagation under RCCI conditions. *Combust Flame* 2015;162(9):3412–26.
- [28] Tekgül B, Kahila H, Karimkashi S, Kaario O, Ahmad Z, Lendormy É, Hyvönen J, Vuorinen V. Large-eddy simulation of spray assisted dual-fuel ignition under reactivity-controlled dynamic conditions. *Fuel* 2021;293:120295.
- [29] Zhong S, Xu S, Bai X-S, Peng Z, Zhang F. Large eddy simulation of n-heptane/syngas pilot ignition spray combustion: ignition process, liftoff evolution and pollutant emissions. *Energy* 2021;121080.
- [30] Peters N. Laminar diffusion flamelet models in non-premixed turbulent combustion. *Prog Energy Combust Sci* 1984;10(3):319–39.
- [31] Xu S, Zhong S, Pang KM, Yu S, Jangi M, Bai X-s. Effects of ambient methanol on pollutants formation in dual-fuel spray combustion at varying ambient temperatures: A large-eddy simulation. *Appl Energy* 2020;279:115774.
- [32] Xu S, Zhong S, Zhang F, Bai X-S. On element mass conservation in Eulerian stochastic fields modeling of turbulent combustion. *Combust Flame* 2022;239:111577.
- [33] Hadadpour A, Xu S, Zhang Y, Bai X-S, Jangi M. An extended FGM model with transported PDF for LES of spray combustion. *Proc Combust Inst* 2022.
- [34] Decan G, Lucchini T, D'Errico G, Verhelst S. A coupled tabulated kinetics and flame propagation model for the simulation of fumigated medium speed dual-fuel engines. *SAE Technical Paper*, 2019.
- [35] Seddik O, Pandurangi S, Bolla M, Boulouchos K, Srna A, Wright YM. Flamelet generated manifolds applied to Dual-Fuel combustion of lean methane/air mixtures at engine relevant conditions ignited by n dodecane micro pilot sprays. *SAE Technical Paper*, 2019, p. 1163.
- [36] Decan G, Lucchini T, D'Errico G, Verhelst S. A novel technique for detailed and time-efficient combustion modeling of fumigated dual-fuel internal combustion engines. *Appl Therm Eng* 2020;174:115224.
- [37] Van Oijen J, De Goey L. Modelling of premixed laminar flames using flamelet-generated manifolds. *Combust Sci Technol* 2000;161(1):113–37.
- [38] De Goey L, ten Thije Boonkamp J. A flamelet description of premixed laminar flames and the relation with flame stretch. *Combust Flame* 1999;119(3):253–71.
- [39] Xu L, Zhang Y, Tang Q, Johansson B, Yao M, Bai X-S. LES/FGM investigation of ignition and flame structure in a gasoline partially premixed combustion engine. *Proc Combust Inst* 2022.
- [40] Wehrfritz A, Kaario O, Vuorinen V, Somers B. Large eddy simulation of n-dodecane spray flames using flamelet generated manifolds. *Combust Flame* 2016;167:113–31.
- [41] Pickett LM, Bruneaux G, Payri R. Engine combustion network. 2021, Accessed 12 June 2023.
- [42] Masouleh MG, Wehrfritz A, Kaario O, Kahila H, Vuorinen V. Comparative study on chemical kinetic schemes for dual-fuel combustion of n-dodecane/methane blends. *Fuel* 2017;191:62–76.

- [43] Bao H, Akargun HY, Roekaerts D, Somers B. The inclusion of scalar dissipation rate in modeling of an n-dodecane spray flame using flamelet generated manifold. *Combust Flame* 2023;249:112610.
- [44] Bao H, Maes N, Akargun HY, Somers B. Large Eddy Simulation of cavitation effects on reacting spray flames using FGM and a new dispersion model with multiple realizations. *Combust Flame* 2022;236:111764.
- [45] Lu T, Yoo CS, Chen J, Law CK. Three-dimensional direct numerical simulation of a turbulent lifted hydrogen jet flame in heated coflow: a chemical explosive mode analysis. *J Fluid Mech* 2010;652:45–64.
- [46] Bharadwaj N, Rutland C, Chang S-M. Large eddy simulation modelling of spray-induced turbulence effects. *Int J Engine Res* 2009;10(2):97–119.
- [47] Tsang C-W, Trujillo MF, Rutland CJ. Large-eddy simulation of shear flows and high-speed vaporizing liquid fuel sprays. *Comput & Fluids* 2014;105:262–79.
- [48] Kärholm FP. Numerical modelling of diesel spray injection, turbulence interaction and combustion [Ph.D. thesis], Chalmers University of Technology Gothenburg, Chalmers (Sweden); 2008.
- [49] Amsden AA, O'Rourke PJ, Butler TD. KIVA-II: A computer program for chemically reactive flows with sprays. Los Alamos National Laboratory (LANL), Los Alamos, NM (United States); 1989, p. 11560.
- [50] Tsang C-W, Kuo C-W, Trujillo M, Rutland C. Evaluation and validation of large-eddy simulation sub-grid spray dispersion models using high-fidelity volume-of-fluid simulation data and engine combustion network experimental data. *Int J Engine Res* 2019;20(6):583–605.
- [51] O'Rourke PJ. Collective drop effects on vaporizing liquid sprays [Ph.D. thesis], Princeton University, Princeton (United States); 1981.
- [52] Zuo B, Gomes A, Rutland C. Studies of superheated fuel spray structures and vaporization in gdi engines. In: Eleventh international multidimensional engine modeling user's group meeting. 2000.
- [53] Ranz W, Marshall WR, et al. Evaporation from drops. *Chem Eng Progr* 1952;48(3):141–6.
- [54] Ricart L, Xin J, Bower GR, Reitz RD. In-cylinder measurement and modeling of liquid fuel spray penetration in a heavy-duty diesel engine. *SAE Trans* 1997;1622–40.
- [55] Somers B. The simulation of flat flames with detailed and reduced chemical models [Ph.D. thesis], Technische Universiteit Eindhoven, Eindhoven (Netherlands); 1994.
- [56] Yao T, Pei Y, Zhong B-J, Som S, Lu T, Luo KH. A compact skeletal mechanism for n-dodecane with optimized semi-global low-temperature chemistry for diesel engine simulations. *Fuel* 2017;191:339–49.
- [57] Kahila H, Wehrfritz A, Kaario O, Vuorinen V. Large-eddy simulation of dual-fuel ignition: Diesel spray injection into a lean methane-air mixture. *Combust Flame* 2019;199:131–51.
- [58] Smith GP, Golden DM, Frenklach M, Moriarty NW, Eiteneer B, Goldenberg M, Bowman CT, Hanson RK, Song S, Gardiner WC, Lissianski VV, Qin Z. GRI-3.0 mechanism. 2022, <http://combustion.berkeley.edu/gri-mech/>.
- [59] Bilger R, Stårner S, Kee R. On reduced mechanisms for methane-air combustion in nonpremixed flames. *Combust Flame* 1990;80(2):135–49.
- [60] Vasavan A, de Goeij P, van Oijen J. A novel method to automate FGM progress variable with application to igniting combustion systems. *Combust Theory Model* 2020;24(2):221–44.
- [61] Floyd J, Kempf AM, Kronenburg 1 A, Ram R. A simple model for the filtered density function for passive scalar combustion LES. *Combust Theory Model* 2009;13(4):559–88.
- [62] Pierce CD, Moin P. A dynamic model for subgrid-scale variance and dissipation rate of a conserved scalar. *Phys Fluids* 1998;10(12):3041–4.
- [63] Lam S-H, Goussis DA. Understanding complex chemical kinetics with computational singular perturbation. *Symp Int Combust* 1989;22(1):931–41.
- [64] Goussis DA, Im HG, Najm HN, Paolucci S, Valorani M. The origin of CEMA and its relation to CSP. *Combust Flame* 2021;227:396–401.
- [65] Lu T, Yoo C, Chen J, Law C. Analysis of a turbulent lifted hydrogen/air jet flame from direct numerical simulation with computational singular perturbation. In: 46th AIAA aerospace sciences meeting and exhibit. 2008, p. 1013.
- [66] Xu C, Ameen MM, Som S, Chen JH, Ren Z, Lu T. Dynamic adaptive combustion modeling of spray flames based on chemical explosive mode analysis. *Combust Flame* 2018;195:30–9.
- [67] Xu C, Park J-W, Yoo CS, Chen JH, Lu T. Identification of premixed flame propagation modes using chemical explosive mode analysis. *Proc Combust Inst* 2019;37(2):2407–15.
- [68] Xu C, Poludnenko AY, Zhao X, Wang H, Lu T. Structure of strongly turbulent premixed n-dodecane-air flames: Direct numerical simulations and chemical explosive mode analysis. *Combust Flame* 2019;209:27–40.
- [69] Pickett LM, Genzale CL, Bruneaux G, Malbec L-M, Hermant L, Christiansen C, Schramm J. Comparison of diesel spray combustion in different high-temperature, high-pressure facilities. *SAE Int J Engines* 2010;3(2):156–81.
- [70] Akkurt B. Modelling multi-pulse diesel injection with flamelet generated manifolds [Ph.D. thesis], Technische Universiteit Eindhoven, Eindhoven (Netherlands); 2019.
- [71] Goodwin DG, Speth RL, Moffat HK, Weber BW. Cantera: An object-oriented software toolkit for chemical kinetics, thermodynamics, and transport processes. 2021, <http://dx.doi.org/10.5281/zenodo.4527812>, <https://www.cantera.org> Version 2.6.0a2.
- [72] Westbrook CK. Chemical kinetics of hydrocarbon ignition in practical combustion systems. *Proc Combust Inst* 2000;28(2):1563–77.
- [73] Borghesi G, Krisman A, Lu T, Chen JH. Direct numerical simulation of a temporally evolving air/n-dodecane jet at low-temperature diesel-relevant conditions. *Combust Flame* 2018;195:183–202.
- [74] Benajes J, Payri R, Bardi M, Martí-Aldaraví P. Experimental characterization of diesel ignition and lift-off length using a single-hole ECN injector. *Appl Therm Eng* 2013;58(1–2):554–63.
- [75] Mastorakos E. Ignition of turbulent non-premixed flames. *Prog Energy Combust Sci* 2009;35(1):57–97.
- [76] De Goeij P, ten Thijs Boonkamp J. A mass-based definition of flame stretch for flames with finite thickness. *Combust Sci Technol* 1997;122(1–6):399–405.
- [77] Stahl G, Warnatz J. Numerical investigation of time-dependent properties and extinction of strained methane- and propane-air flamelets. *Combust Flame* 1991;85(3–4):285–99.
- [78] Xue Q, Som S, Senecal P, Pomraning E. A study of grid resolution and SGS models for LES under non-reacting spray conditions. In: ILASS Americas, 25th annual conference on liquid atomization and spray systems. 2013.
- [79] Desantes J, García-Oliver JM, Novella R, Pérez-Sánchez E. Application of a flamelet-based CFD combustion model to the LES simulation of a diesel-like reacting spray. *Comput & Fluids* 2020;200:104419.
- [80] Maes N, Meijer M, Dam N, Somers B, Toda HB, Bruneaux G, Skeen SA, Pickett LM, Manin J. Characterization of Spray A flame structure for parametric variations in ECN constant-volume vessels using chemiluminescence and laser-induced fluorescence. *Combust Flame* 2016;174:138–51.
- [81] Desantes JM, López JJ, García-Oliver JM, López-Pintor D. Experimental validation and analysis of seven different chemical kinetic mechanisms for n-dodecane using a rapid compression-expansion machine. *Combust Flame* 2017;182:76–89.
- [82] Sim HS, Maes N, Weiss L, Pickett LM, Skeen SA. Detailed measurements of transient two-stage ignition and combustion processes in high-pressure spray flames using simultaneous high-speed formaldehyde PLIF and schlieren imaging. *Proc Combust Inst* 2021;38(4):5713–21.
- [83] Borghesi G, Mastorakos E, Cant RS. Complex chemistry DNS of n-heptane spray autoignition at high pressure and intermediate temperature conditions. *Combust Flame* 2013;160(7):1254–75.
- [84] Ong JC, Pang KM, Walther JH. Prediction method for ignition delay time of liquid spray combustion in constant volume chamber. *Fuel* 2021;287:119539.
- [85] Pei Y, Som S, Pomraning E, Senecal PK, Skeen SA, Manin J, Pickett LM. Large eddy simulation of a reacting spray flame with multiple realizations under compression ignition engine conditions. *Combust Flame* 2015;162(12):4442–55.
- [86] Maes N, Sim HS, Weiss L, Pickett L. Simultaneous high-speed formaldehyde PLIF and schlieren imaging of multiple injections from an ECN spray D injector. In: Internal combustion engine division fall technical conference, vol. 84034. American Society of Mechanical Engineers; 2020, V001T05A001.
- [87] Dahms RN, Paczko GA, Skeen SA, Pickett LM. Understanding the ignition mechanism of high-pressure spray flames. *Proc Combust Inst* 2017;36(2):2615–23.
- [88] Zhang Y, Xu S, Zhong S, Bai X-S, Wang H, Yao M. Large eddy simulation of spray combustion using flamelet generated manifolds combined with artificial neural networks. *Energy and AI* 2020;2:100021.